Subsurface Structures Around the Subducting Seamount Illuminated by Local Earthquakes at the Off-Ibaraki Region, Southern Japan Trench

Shinji Yoneshima[1], Kimihiro Mochizuki[2], Tomoaki Yamada[2], and Masanao Shinohara[2]

[1]Earthquake Research Institute, University of Tokyo
[2]University of Tokyo

November 22, 2022

Abstract

The off-Ibaraki region is a convergent margin at which a seamount subducts. An intensive event location was performed around the subducting seamount to reveal the regional seismotectonics of this region. By applying a migration-based event location to an Ocean Bottom Seismic network record of both P- and S-waves, over 20,000 events were determined in the off-Ibaraki region below ˜M4. The seismicity showed clear spatiotemporal patterns enough to identify the seismicity changes and geometry of the interface. At the updip side, the shallow tectonic tremors and earthquakes are shown to be spatially complementary bounded by an updip limit of the seismogenic zone. At the downdip side, a semicircular low-seismicity zone was identified, which is possibly a rupture area of the Mw7.9 event. The event depth profile exhibited a gently sloped planar downdip interface subparallel to the subducting slab. This plane appears to be stably active from 2008 to 2011. Comparison with the active source seismic survey profiles exhibits that this planar downdip interface is several kilometers deeper than the top of the oceanic crust. After the Mw7.9 event, a high-angle downdip seismic interface was activated above the planar interface. Further, below the planar downdip interface, broadly scattered events occurred with a swarm manner. We successfully illuminated the complicated subsurface structures around the subducting seamount. It is suggested that most of the event occur along or below the plate interface as the top of the oceanic crust.

Hosted file

`essoar.10510899.1.docx` available at https://authorea.com/users/540108/articles/600125-subsurface-structures-around-the-subducting-seamount-illuminated-by-local-earthquakes-at-the-off-ibaraki-region-southern-japan-trench

Subsurface Structures Around the Subducting Seamount Illuminated by Local Earthquakes at the Off-Ibaraki Region, Southern Japan Trench

Shinji Yoneshima[1], Kimihiro Mochizuki[1], Tomoaki Yamada[1], and Masanao Shinohara[1]

[1]Earthquake Research Institute, University of Tokyo.

Corresponding author: Shinji Yoneshima (shinji@eri.u-tokyo.ac.jp)

Key Points:

- Over 20,000 events are determined using Ocean Bottom Seismometers around the subducting seamount.
- Small events and shallow tectonic tremor are spatially complementary with each other bounded by the updip limit of the seismogenic zone.
- Two seismically active interfaces are identified around the top of the oceanic crust and below it.

Abstract

The off-Ibaraki region is a convergent margin at which a seamount subducts. An intensive event location was performed around the subducting seamount to reveal the regional seismotectonics of this region. By applying a migration-based event location to an Ocean Bottom Seismic network record of both P- and S-waves, over 20,000 events were determined in the off-Ibaraki region below ~M4. The seismicity showed clear spatiotemporal patterns enough to identify the seismicity changes and geometry of the interface. At the updip side, the shallow tectonic tremors and earthquakes are shown to be spatially complementary bounded by an updip limit of the seismogenic zone. At the downdip side, a semicircular low-seismicity zone was identified, which is possibly a rupture area of the Mw7.9 event. The event depth profile exhibited a gently sloped planar downdip interface subparallel to the subducting slab. This plane appears to be stably active from 2008 to 2011. Comparison with the active source seismic survey profiles exhibits that this planar downdip interface is several kilometers deeper than the top of the oceanic crust. After the Mw7.9 event, a high-angle downdip seismic interface was activated above the planar interface. Further, below the planar downdip interface, broadly scattered events occurred with a swarm manner. We successfully illuminated the complicated subsurface structures around the subducting seamount. It is suggested that most of the event occur along or below the plate interface as the top of the oceanic crust.

Plain Language Summary

In the off-Ibaraki region, where a seamount subducts, a large number of small earthquakes occurred as aftershocks of the Mw7.9 thrust event. We applied a new event location technique to the Ocean Bottom Seismometer record, and we determined more than 20,000 of these aftershocks. The obtained seismicity shows that the small earthquakes and tectonic tremors are located close to each other with little spatial gap. At the downdip portion, a semicircular low seismicity zone was identified, possibly a rupture area of the Mw7.9 event. Along the depth cross section, a simple planar downdip seismic plane was identified where the seismicity has been stably high from 2008 to 2011. After the Mw7.9 event, above the planar downdip interface, a high-angle downdip seismic plane was activated at around the depth of the plate interface. Below the planar downdip interface, earthquakes occurred with a swarm manner. We successfully illuminated the complicated subsurface structures around the subducting seamount. This planar seismic plane is several kilometers deeper than the top of the oceanic crust. Our results suggest that most of the event occur along or below the plate interface as the top of the oceanic crust.

1 Introduction

1.1. Tectonics at the off-Ibaraki region

The off-Ibaraki region is a convergent margin located at the south of northeastern Japan. Accompanying the subduction of the North Pacific Plate beneath the North American plate, M6 to M7 events occurs periodically with an interval of approximately a few decades (Earthquake Research Committee, 2012; Matsumura, 2010). In early 2000, an intensive seismic survey was performed in this region, and the subducting seamount was identified (Mochizuki et al., 2008). Subsequently, attention has been devoted to this region regarding the tectonics of the seamount subduction, focusing on the role of the seamount subduction for large earthquakes (Bassett et al., 2015; Kubo et al., 2013; Kubo & Nishikawa, 2020; Nakatani et al., 2015; Sun et al., 2020; Wang & Bilek, 2014). Wang and Bilek (2014) suggested the presence of microfractures off the plate interface as a result of the seamount subduction.

In spite of these studies, the possible consequence of the seamount subduction to the occurrence of earthquakes is not well constrained yet. Sun et al. (2020) incorporated the small earthquake distribution from Ocean Bottom Seismometrer (OBSs) and showed that part of the small earthquakes occurs at the wake of the seamount. Nevertheless, because the number of events is still limited and also the event location uses one-dimensional velocity structure (1-D), it is still insufficient to discuss the depth of these events with respect to the plate interface. The accurate event locations for large number of earthquakes are required to further develop the understanding of the seamount subduction tectonics with respect to earthquakes.

In 2011, as the largest aftershock of the 2011 Tohoku-oki earthquake, an Mw7.9 event occurred approximately 30 min after the mainshock. The rupture was initiated at the deeper portion and propagated toward updip (Honda et al., 2013; Kubo et al., 2013; Suzuki et al., 2020). The rupture terminated around the rim of the subducting seamount (Kubo et al., 2013). Nakatani et al. (2015) determined the epicenters of events. They reported that the seismicity was considerably enhanced after the Mw7.9 event using OBSs, especially at the northern part of the seamount. The located events, however, do not provide the event depth information, since events were constrained on the plate interface of the three-dimensional (3-D) velocity model used for the event location. The reliable 3-D event locations using OBSs are expected to provide an integrated understanding of the regional tectonics regarding the large event and subducting seamount as well as the occurrence of shallow tectonic tremors. This study reveals the precise seismicity of small earthquakes at the off-Ibaraki region and discusses its relationship with other tectonics, including the shallow tectonic tremor, seamount, and Mw7.9 event, around the off-Ibaraki region.

As another remarkable tectonic feature of this region, several years after the Mw7.9 event, a shallow tectonic tremor was identified at the off-Ibaraki region in and around the subducting seamount (Nishikawa et al., 2019). Kubo and Nishikawa (2020) discussed that the rupture of the Mw7.9 event in 2011 terminated at the forefront side of the seamount, and the shallow tectonic tremor begin to occur at the updip. Sun et al. (2020) showed that small earthquakes are present between the coseismic rupture area of the Mw7.9 event and the shallow tectonic tremor. Sun et al. (2020) also suggested that the rupture termination can be attributed to the increased effective normal stress at the forefront of the subducting seamount acting as a barrier.

To better elucidate the seamount subduction tectonics, a large number of accurately located small earthquakes are definitely helpful. For example, previous studies suggested that micro fractures in the overriding plate may evolve owing to the seamount subduction (e.g., Chesley et al., 2021; Wang & Bilek, 2011, 2014). Shaddox and Schwartz (2019) reported the occurrence of highly correlated earthquakes above the plate boundary at the northern Hikurangi Margin. Recent studies showed that event locations are broadly scattered in the oceanic crust around the subducting seamount (Central Ecuador by Collot et al., 2017; Northern Hikurangi Margin by Yarce et al., 2019). The identification of events off the plate interface to illuminate subsurface structures is essential to further understand the seamount subduction tectonics.

1.2. Migration-based event location workflow

In order to accurately determine the location of small earthquakes, the use of the OBSs are necessary. One of the advantages of using OBSs to monitor subduction zone earthquakes is fine event location accuracy beneath or in the vicinity of an OBS network around the seismogenic zone because the location error tends to be smaller beneath or around the seismic network (Bartal et al., 2000; Lilwall & Francis, 1978; Uhrhammer, 1980). By using OBSs, a variety of hypocenter distribution patterns has been reported in subduction zones (Hino et al., 2000, 2009; Léon-Ríos et al., 2019; Mochizuki et al., 2010; Sachpazi et al., 2020; Sakai et al., 2005; Sgroi et al., 2021; Shinohara et al., 2005; Yarce et al., 2019; Yoneshima et al., 2005).

To deal with large numbers of events efficiently, Yoneshima and Mochizuki (2021) proposed a migration-based event location method without manually picking arrival times. This method is rather versatile for any seismological domains but particularly demonstrated the OBS's record at the off-Ibaraki region for events occurred during October 2010–February 2011. This method enabled the processing of quite a few events in a reasonable amount of effort and time. At present, this method is not applied yet to large numbers of dataset. This study will demonstrate this event location method for the first time to the large numbers of real event data by Yoneshima and Mochizuki (2021).

On the other hand, for the event location accuracy as a bias from the true event location, the accurate input velocity model is crucial. However, constructing a reliable velocity model has still been a challenge, especially for the S-wave velocity model. For the migration-based event location method, an accurate 3-D velocity model is particularly desired for better beamforming perspective. For obtaining a P-wave velocity structure, active source seismic surveys such as wide-angle refraction surveys or seismic tomography can provide a detailed two-dimensional (2-D) P-wave velocity structure (Arai et al., 2017; Nakahigashi et al., 2012; Nakanishi et al., 2008) or occasionally a 3-D velocity structure (Obana et al., 2009) can be used. Such a fine velocity model directly compares the event location with velocity structure (Arai et al., 2017). While the P-wave velocity structure is well determined, the S-wave velocity structure remains uncertain.

In case of a S-wave velocity structure, usually, a constant Vp/Vs ratio is assigned to the P-wave velocity model, such as 1.73 for the entire velocity model, including a sediment layer while applying a station correction (e.g., Yoneshima et al., 2005). This naïve assumption of Vp/Vs value potentially results in the location bias when the assumed Vp/Vs ratio is departed from the true value. Therefore, a reliable initial S-wave velocity model is needed for both the migration-based event location and accurate event location purposes. Recently, Yamaya et al. (2021) derived the S-wave velocity structure using Rayleigh waves for sediment layer and the upper crust. To cover wider depth range for the entire event location depths, the present study estimates an average Vp/Vs ratio below the basement of the sediment layer (hereafter denoted as K_1) in order to obtain the representative value of the Vp/Vs ratio below the sediment layer.

1.3. Objective of this study

The present study addresses two objectives. First, this study defines a comprehensive event location workflow of the migration-based event location, and demonstrates the method to large numbers of events at the off-Ibaraki region in and around a subducting seamount (Mochizuki et al., 2008). This workflow contains the determination of the K_1 for the accurate event location. Second, we describe the spatiotemporal seismicity patterns at the off-Ibaraki region and its relationships with other tectonics such as the seamount, Mw7.9 event, and the shallow tectonic tremor. Based on the obtained spatiotemporal seismicity patterns, the illuminated subsurface structures associated with the regional tectonics is discussed.

2 Data

2.1. OBS experiment

The OBS experiment was conducted from 17 October 2010 to 19 September 2011 (~11 months) at the off-Ibaraki region. The layout of the OBS network is shown in Figure 1. In total, 31 OBSs were deployed, equipped with three-component 1-Hz geophones. The seismic record was acquired continuously at a 200-Hz sampling rate. As a notable feature of this OBS experiment, the OBS network geometry was configured with a high-density spacing of 6 km. By contrast, the usual OBS seismic spacing is ~20–30 km (e.g. Shinohara et al., 2012). This high-density OBS network is expected to detect small and shallow earthquakes in the overriding plate and events along and below the plate boundary. The other notable feature of this OBS experiment is that around the middle of the OBS experiment, the 2011 Tohoku-oki earthquakes occurred, with the largest aftershock of Mw7.9 event in the study area. The seismicity was continuously monitored before and after the 2011 Tohoku-oki earthquake (Nakatani et al., 2015).

The overall spatiotemporal OBS availability is good regarding the 2011 Tohoku-oki earthquake. The observation period for each OBS is is mainly divided into two groups: one spanning the entire period and the other started monitoring in the middle of February 2011 (Figure S1). Exceptionally, some OBSs were retrieved in March 2011 owing to the occurrence and emergent analysis of the 2011 Tohoku-oki earthquake (Shinohara et al., 2011, 2012).

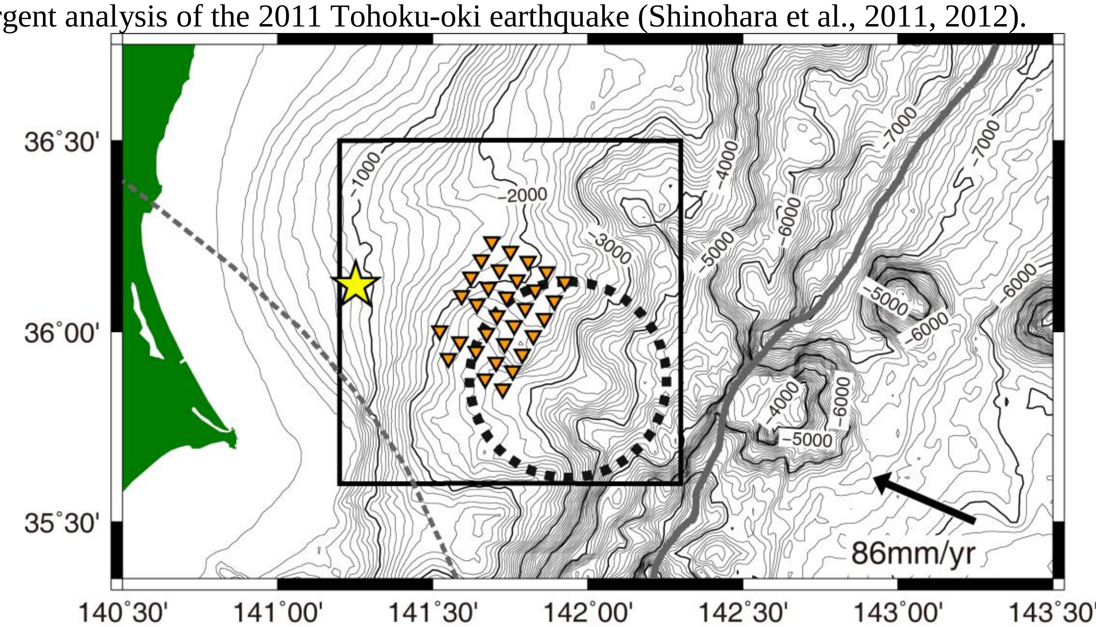

Figure 1. Map view of the study area at the off-Ibaraki region. The black rectangle represents the study area of this study. The inverted triangles denote the OBSs. The bold dashed circle presents the subducting seamount (Mochizuki et al., 2008). The yellow star represents the JMA hypocenter of the Mw7.9 event. The dashed gray line shows the PHS limit (Nakajima et al., 2009). The bold dark gray line presents the trench axis. The bold arrow and the value denote the relative plate motion and the convergence rate between the Pacific plate and the North American plate (DeMets et al., 1990).

2.2. 3-D velocity model

The P-wave 3-D velocity model is shown in Figure 2, together with the OBS locations. This model is constructed after compiling the existing seismic velocity surveys: wide-angle refraction surveys conducted by Miura et al. (2003), Nakahigashi et al. (2012) and land seismic tomography reported by Matsubara and Obara (2011). A plate interface depth map with a subducting seamount is developed on the basis of the report by Shinohara et al. (2011) and superimposed with the seamount depth obtained from the report by Mochizuki et al. (2008). The horizontal and vertical grid sizes of the velocity model are 400 and 200 m, respectively.

The S-wave velocity structure was addressed separately in two parts. Each set had a different Vp/Vs ratio: one in the sediment layer above the basement (hereafter denoted as K_0) and the other in the consolidated layer below the basement (K_1). The K_0 was estimated for each OBS site using the PS-converted waves and is shown in Figure S2. This estimated K_0 was directly embedded into the S-wave velocity structure, while the conventional method used a constant Vp/Vs ratio velocity model to apply a static station correction. Below the basement, in the consolidated layer, a uniform Vp/Vs ratio value of 1.73 was tentatively assumed as K_1. After setting up the velocity model, the synthetic travel times for P- and S-wave were computed by solving the Eikonal equation using a fast-marching method (de Kool et al., 2006) following the report by Yoneshima and Mochizuki (2021). This tentative velocity structure is later optimized and its details are described in the next section.

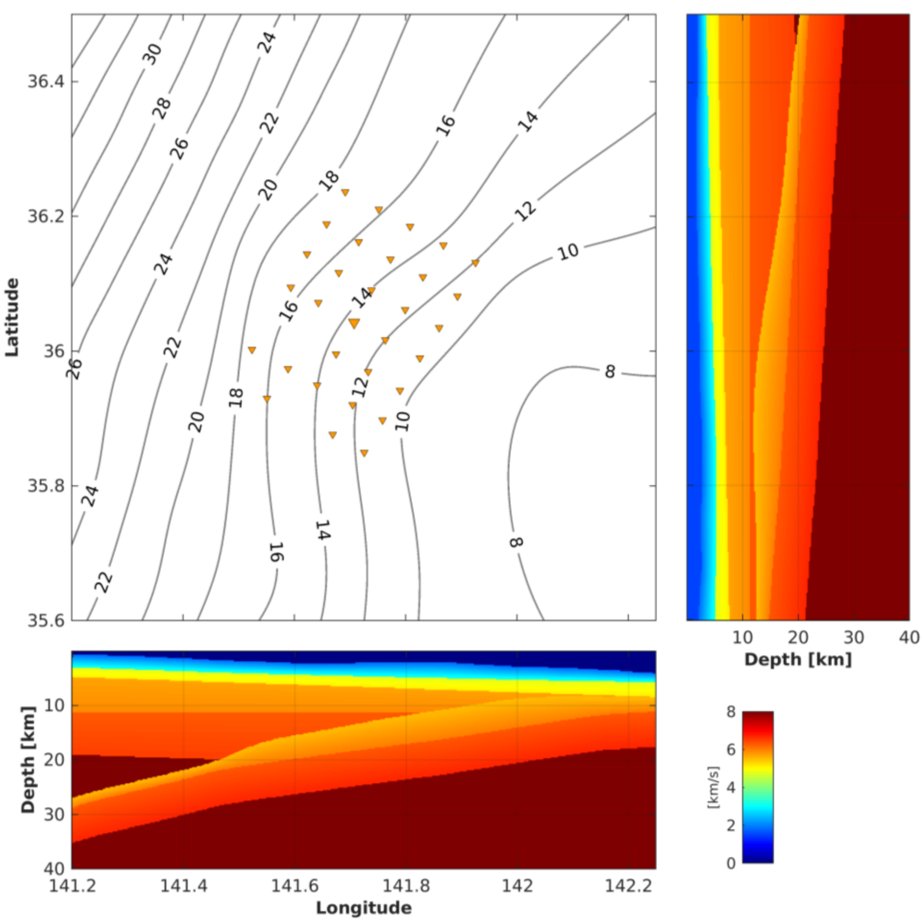

Figure 2. Velocity structure model used in this study. (Top left) Plain map view with the plate depth contour, with labels presented in kilometers. The inverted triangles denote the OBS locations.

Station names are shown in Figure S1, namely from SMD001 to SMD035. The large inverted triangle denotes the reference OBS of SMD018 as the center of the OBS array for the cross-section views in the bottom and right panel. (Bottom and right) Cross sections of the P-wave velocity structure intersecting the reference SMD018.

3. Comprehensive workflow for migration-based event location

This section describes overall workflow of the event location. This workflow is particularly defined for the migration-based event location to reliably determine the event location, including the optimization of the Vp/Vs ratio of the input velocity model. Figure 3 shows the entire workflow of the event location processing from the event detection to event finalization.

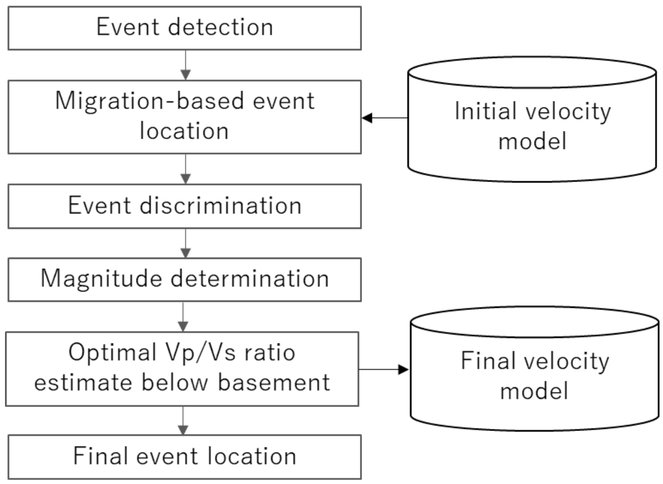

Figure 3. Entire workflow to process a migration-based event location, including the Vp/Vs ratio optimization of a velocity model.

3.1. Event location procedure

This section describes the event location procedure up to the finalization of the events, including the optimization of the K_1. First, event detection is performed. For the event detection, the present study applied a conventional short-time-average/long-term-average (STA/LTA) triggering method combined with an amplitude threshold. The amplitude threshold was set to $5e^{-6}$ m/s. In total, 87,084 events were detected during the observation period. Note that the seismicity at the Tohoku-oki region was quite high during the OBS experiment. This resulted in the contamination of these regional events outside the study area, together with the detection of local events in the study area. At this stage, both local and nonlocal events are included in the event list that are discriminated later.

After the event detection, a migration-based event location was applied for all the detected events by applying the method proposed by Yoneshima and Mochizuki (2021), including a station correction and an error bar calculation. A 4-Hz high-pass filter was used to suppress the low-frequency noise. Using the synthetic travel times computed in the previous section, the migration-based event location method was applied following the report by Yoneshima and Mochizuki (2021). After the event location of all the detected events, event discrimination was performed to reject the nonlocal events such as the regional/teleseismic events. This event discrimination was performed via a visual inspection of waveforms by human eyes. Events that are located farther than the trench axis were also excluded. After rejecting the nonlocal events, 22,562 events were identified as the local events in the study area. The final event dataset was selected with error bars of <6 km as a 95% confidence interval of the semimajor axis or the error bar. The number of selected events was 21,242. The waveform example is shown in Figure S3.

Then we determined event magnitudes using Watanabe's formula (Watanabe, 1971). This method is widely applied in the OBS study (e.g. Obana et al., 2021). A magnitude correction is performed using the JMA event magnitudes. In total, 3448 JMA events were matched with the OBS event list. The magnitude correction was performed via a simple bias correction, parameterized by a constant offset (Figure S4). Notably, the event magnitude tends to be saturated at OBS magnitude ≈ 4 because of the S-wave amplitude saturation. When estimating a correction value, these large event magnitudes were rejected (the dark gray stars presented in Figure 4). The corrected event magnitude equation is obtained as follows:

$$M_{OBS}^{corrected} = \frac{\log max\left(A_x, A_y, A_z\right) + 1.73 \log r + 2.5}{0.85} - 1.75. \quad (1)$$

This equation applies to all the local events that are not listed in the JMA catalog.

Then, we optimized the velocity model particularly K_1 to obtain the accurate event location. As a procedure, we applied a 1-parameter grid search inversion to find the optimal K_1. For the objective function, we used a coherence value using both P- and S-wave (Grigoli et al., 2014; Yoneshima & Mochizuki, 2021). The objective function is defined as follows as a summation for the number of events;

$$\mathrm{f}(K_1) = \frac{1}{ne}\sum_{i=1}^{ne} coherence_i(x, y, z, T0; K_1), \quad (2)$$

, where ne is the number of events, $x, y, z, T0$, are the hypocenter parameters, and K_1 is the average Vp/Vs ratio below the basement of the sediment layer. A maximum objective function in equation (2) is sought through a grid search in the range from 1.73 to 1.83. For the inversion, we selected 1050 events to reduce the computation time. These events were sampled from wide range of the study area to avoid the spatial bias. After the grid search inversion, the optimal K_1 was estimated as 1.74 (Figure 4). Using the estimated value, the final event locations is determined, applying to all the local event dataset.

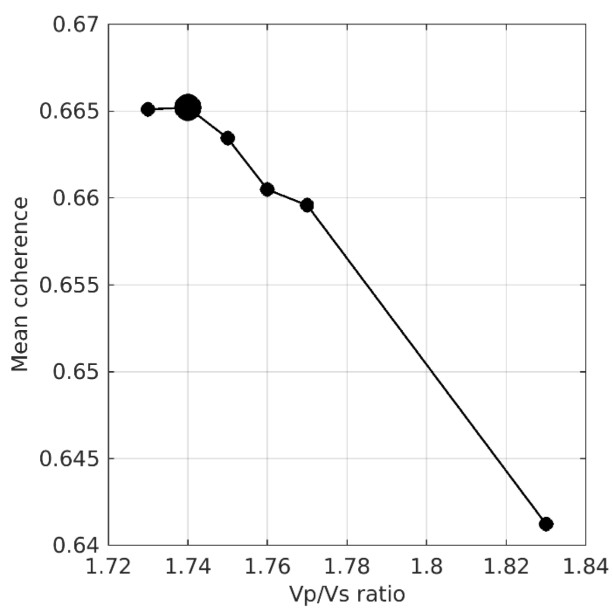

Figure 4. The 1-parameter grid search inversion for coherence. Small solid circles are the tested average Vp/Vs ratio below the basement of the sediment layer. The large solid circle is the optimal value.

3.2. Event detection limit analysis

To facilitate the identification of the spatial variation of the seismicity in the study area, we evaluated the event detection capability for both upper and lower limit.

3.2.1. Upper detection limit

The OBS event magnitude begins to saturate at M ≈ 4, as shown in Figure 5. This is because of the S-wave saturation as its amplitude is approximately one order of magnitude greater than that of the P-wave. This waveform saturation constrains the upper limit of the event detection.

3.2.2. Lower detection limit

The lower limit of the event detection is known to be a function of the focal distance. Accordingly, the lower detection limit is not a constant value in general. We defined the lower detection limit at the furthermost location of the study area from the center of the OBS network.

The relationship between the waveform amplitude and event magnitude in this study was given in equation (1). While this equation is originally used for determining the event magnitude, we use this formula to evaluate the magnitude detection limit for a given waveform amplitude. Using Watanabe's formula, the lower limit of event magnitude detection is given as

$$M^{lower} = \frac{log(A^{threshold}) + 1.73\, log\, r + 2.5}{0.85} - 1.75, \tag{3}$$

where M^{lower}, $A^{threshold}$, and r are the lower limit of event magnitude, the amplitude threshold at the time of the event detection, and the focal distance, respectively. When the focal distance is defined from the center of the OBS network to the event along the raypath of the given velocity models, M^{lower} is readily calculated. Figure 5 compares the event data and curve obtained using equation (3). A raypath length of the P-wave from the source to SMD018 was used for the distance calculation. The real event-detection lower limit agrees well with the theoretical curve obtained using equation (3).\

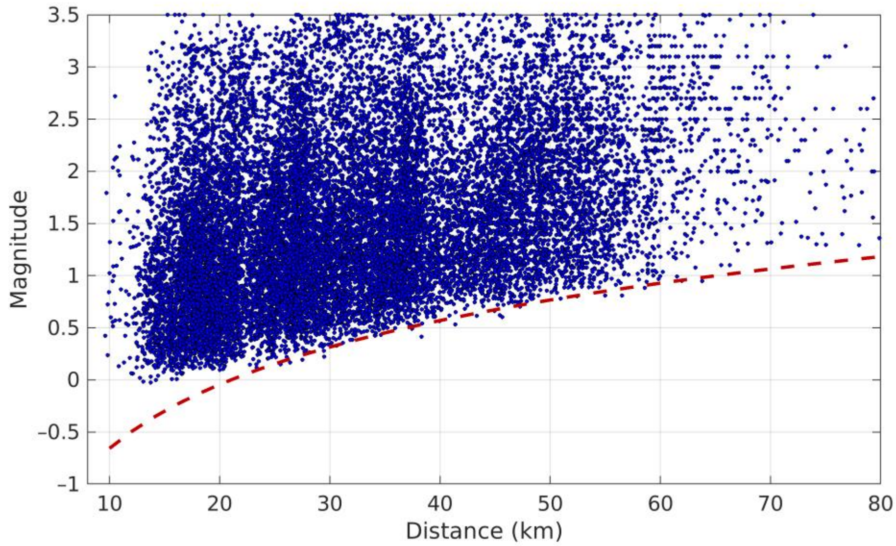

Figure 5. Event magnitudes and focal distance from SMD018. The blue dots represent the located events. The dashed red curve is the event detection curve obtained using equation (3).

Next, this event-detection lower limit was projected into the space in the study area. Figure 6 shows that ~40 km is the lower limit of the event depth distribution in this study area. At a depth of 40.2 km, it is shown that the event detection at the corner of the plan view is approximately M1.

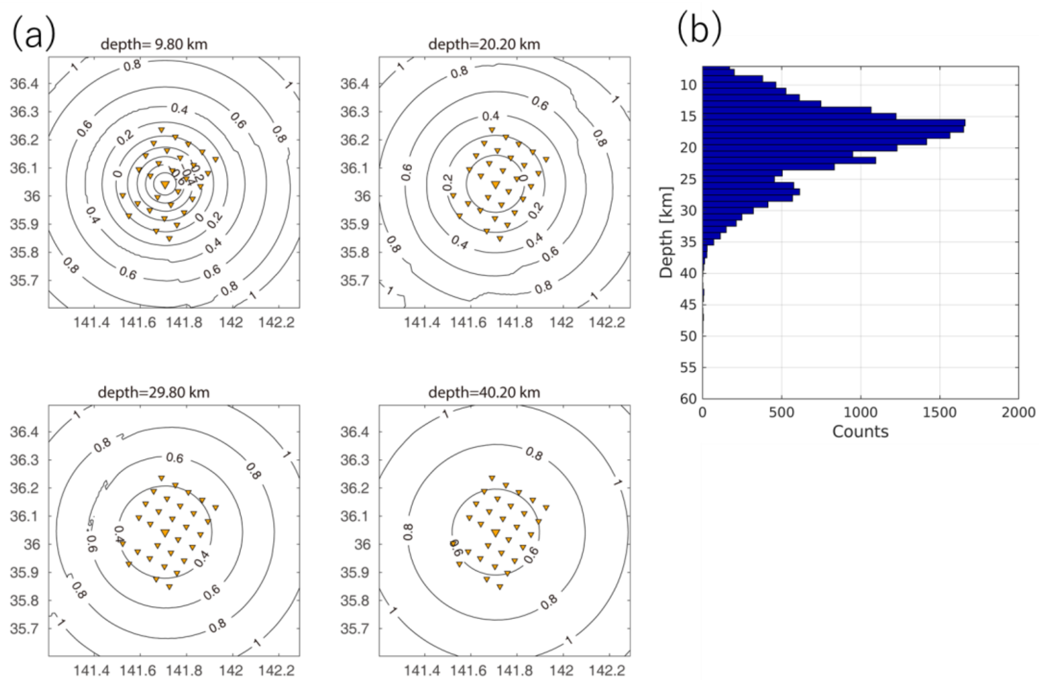

Figure 6. (a) Spatial variation of the event-detection lower limit. Plan view for depth = 9.8, 20.2, 29.8, and 40.2 km. (b) Event depth histogram.

One factor that potentially biases the detection lower limit is the effect of radiation pattern: when a double couple or any angular-dependent energy is radiated from a source, it will deteriorate the magnitude estimate. We believe this effect is not severe because it is reported that for a high-frequency content waveform in the order of Hertz or greater, like observed in this study, the radiation pattern of P- and S-wave becomes mild because of the scattering effect (Takemura et al., 2015, 2016). Therefore, we conclude that the event-detection lower limit of the study area is approximately M1 in this study area.

The temporal variation of the event magnitude distribution is examined using the M-T diagram (Figure S5). At the time of the Tohoku-oki earthquake on 11 March 2011, the event detection capability was degraded until the end of March. This is because of the occurrence of tremendous amounts of aftershocks in a swarm manner inside and outside the study area, resulting in a simultaneous temporal overlap of earthquakes recorded using OBS. It should be noted that even in this swarm period, there is no substantial change of error bar, suggesting that the quality of the successfully located event is not degraded over time.

4. Results

The final result of the migration-based event distribution is shown in Figure 7. As final qualification, we adopted events within the ±6-km error bar as the 95% confidence interval. As a result, in total 21,242 events were successfully located. Among these 21,242 events, 93.6 % of events are less than ±2.0 km of error bar (Figure S6).

4.1. Spatial distribution of hypocenters

The seismicity exhibits an evident spatial pattern where the seismicity is high or low in the study area. Some of the low-seismicity zones have a patchy circular shape. Some of these low seismicity zones are located at the seaward outside the OBS network. Notably, as has been evaluated, the event-detection lower limit is approximately M1 within the entire study area down to 40-km depth; hence, the presence of a low-seismicity zone is real during the observation period. Such spatial variation of the seismicity is more visible in the heat map of the event counts and energy count (Figure 8).

The most remarkable low-seismicity zone lies beneath the OBS network with a semicircular shape. The size of this low-seismicity zone is ~30 × 25 km which is comparable with the size of the OBS network. Remarkably, even after the largest Mw7.9 aftershock in the study area, considerably low seismicity was observed during the observation period.

The seismicity is high toward the updip from this semicircular low-seismicity zone. The seismicity is relatively higher on the northern side compared with the southern side. The event depth of this high-seismicity region is ~15–20 km, which is significantly greater than the plate interface depth at approximately 10 km. This event depth offset from the plate interface is discussed in detail in the next Discussion section.

Further seaward from this high-seismicity zone, the seismicity becomes quite low. The boundary of this seismicity change is subparallel with the isocontour of the plate interface depth of ~10 km. We define this seismicity change boundary at ~10 km plate interface depth as the updip limit of the seismogenic zone.

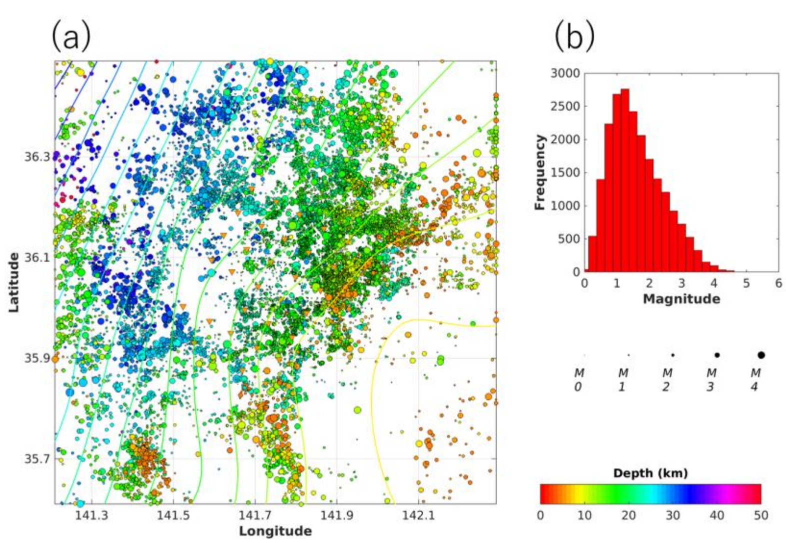

Figure 7. (a) Plan view of the final hypocenter distribution using the estimated Vp/Vs ratio. The solid colored circles represent the events according to the event depth. The solid contour lines present the depth of the plate boundary of the velocity model (Figure 2). The events presented in this plan view are plotted from deeper to shallower events. (b) Histogram of event magnitude.

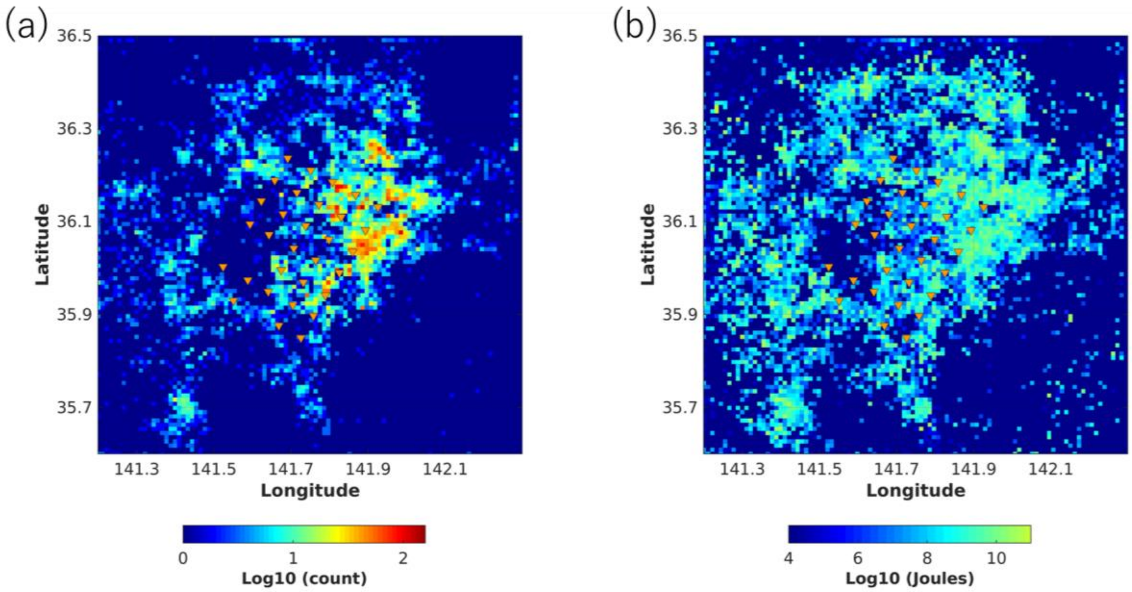

Figure 8. (a) Heat map of the event distribution for a number of events. (b) Heat map of the sum of event energy. The size of the grid is1 km × 1 km.

4.2. Seismicity change bounded by the occurrence of the Mw7.9 event

As shown in the M-T diagram presented in Figure S5, the seismicity was continuously monitored before and after the 2011 Tohoku-oki earthquakes. This enables us to examine the temporal variation of the seismicity.

A temporal variation of the seismicity is shown in Figure 9. Before the occurrence of the largest Mw7.9 aftershock, the event distribution showed a simple planar downdip trend. Hereafter we call this interface the planar downdip interface. After the Mw7.9 event, the seismicity became quite high and exhibited a significant depth variation. Especially, the seismicity was high for both the shallower portion and a deeper portion from this dipping plane. This seismicity after the Mw7.9 event is consistent with the studies reported by Shinohara et al. (2011, 2012) (Figure S7).

The shallower portion of the activated seismicity after the Mw7.9 event shows a high-angle dipping plane close to the updip limit of the seismogenic zone. This updip portion of the shallow seismicity was steadily active from the Mw7.9 event till the end of the OBS experiment.

Meanwhile, for the deeper portion below the planar downdip interface, events are scattered and distributed in a wide area from the updip to the downdip. Further, the seismicity activation of this deeper portion was temporally limited: it became active only soon after the Mw7.9 event. Soon after a few tens of days from the Mw7.9 event, this deeper portion seismicity from the downdip plane became inactive.

In the next Discussion section, based on these new findings of these spatiotemporal seismicity patterns, the seismotectonics at the off-Ibaraki region is discussed together with other seismic and geophysical measurements in this region.

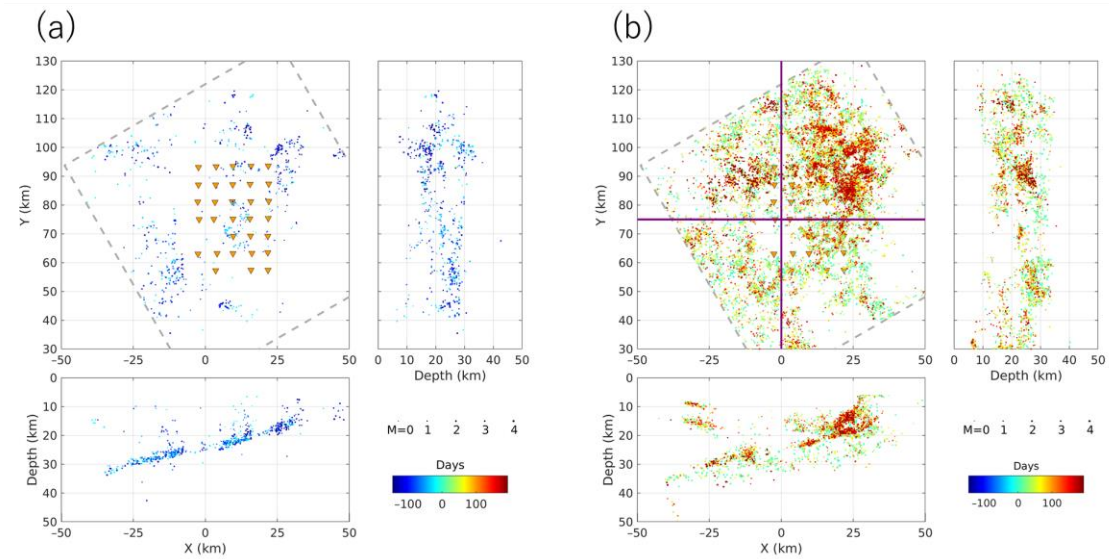

Figure 9. Cross-sectional view of the temporal seismicity variation. (a) Event locations before the Mw7.9 event. Entire spatial range of events was used for cross-section. The color of the events denotes the days after the Mw7.9 event. X is the downdip direction by rotating the horizontal axis by 30° in the anticlockwise direction. The gray dashed rectangular area is the region for cross sections. (b) Event locations after the Mw7.9 event. The purple cross lines are the center line for cross sections. Widths of cross sections in both the X and Y directions are each ±10 km.

5. Discussion

This study determined >20,000 events in a subduction zone around the subducting seamount with a high-density (~6-km spacing) OBS network. Most of the events were determined within ±2 km error bar. To the best of our knowledge, this is an unprecedentedly large number of events by using temporal OBS experiments. This is owing to the dense OBS array, the occurrence of quite a few aftershocks, and the development of an effective event location workflow. This high-density event distribution allows us to identify the local spatial variation of the seismicity with a 1-km grid interval (Figure 8). After the event detection capability analysis, low-seismicity zones are securely identified in the range from approximately M1 to M4 in the study area. Further, the resultant event distribution should be barely biased in space due to the optimization of K_1; therefore, the overall event depth distribution tends to be correct. In addition, the geometry of the interface was reasonably figured out comprising of two distinct seismic interfaces.

These event data allow us to discuss the local seismicity pattern in time and space. The unbiased event distribution enables us to compare with other geophysical survey results. Figure 10 shows the event distribution with the featured tectonics at the off-Ibaraki region: the subducting seamount, relocated hypocenter of the Mw7.9 event by the present study, shallow tectonic tremor from 2016 to 2018, and acoustic GPS (A-GPS) from 2012 to 2016.

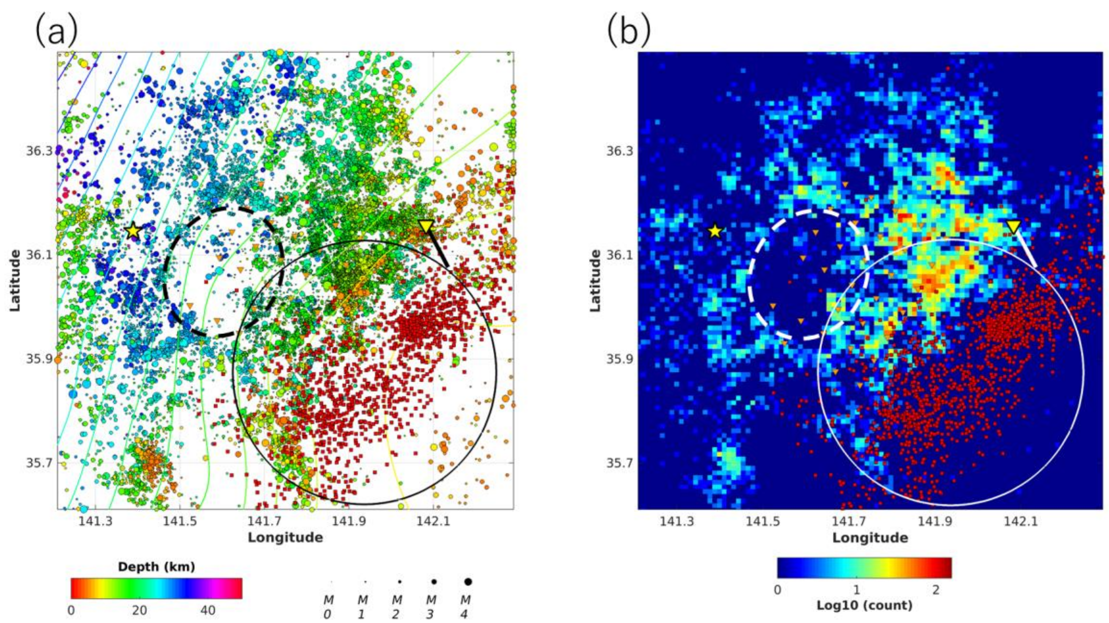

Figure 10. (a) Hypocenter distribution with other geophysical measurements. The solid circles present the events colored according to event depth. The yellow star represents the relocated hypocenter of the Mw7.9 event in this study. A manual time pick was made for this event. The red squares denote the epicenter of the tectonic tremors reported by Nishikawa et al. (2019). The bold dashed circle is the low seismicity zone identified in this study. The large black open circle marks the subducting seamount reported by Mochizuki et al. (2008). The yellow inverted triangle shows the location of A-GPS with a solid line of the displacement vector reported by Honsho et al. (2019). (b) Heat map of the number of events on logarithmic scale. The large white open circle marks the subducting seamount reported by Mochizuki et al. (2008). The white-dashed circle is the low

seismicity zone identified in this study. The yellow inverted triangle shows the location of A-GPS with a solid white line of the displacement vector reported by Honsho et al. (2019). Other symbols such as the hypocenter of the Mw7.9 event and the shallow tectonic tremor and the OBSs are overlaid as same with (a).

The along-dip depth profiles of the event distribution along the seismic survey lines from past researches are shown in Figures 11 and 12. Figure 11 presents the seismic profile of Line EW reported by Mochizuki et al. (2008). Figure 12 shows the seismic survey Line 13 reported by Tsuru et al. (2002), located ~30-km south of Line EW. Both seismic profiles clarify the depth of plate boundary at the updip limit of the seismogenic zone. Each figure exhibits that the shallow tectonic tremors and local events are spatially separated at the updip limit of the seismogenic zone. Most remarkably, it is shown that the majority of the events are distributed several kilometers deeper than the plate interface. The error ellipsoids of each seismic line presented in Figures 11 and 12 are shown in Figures S8 and S9, respectively. Around the updip limit of the seismogenic zone, the maximum error bar as the 68% confident interval is ~0.4 km, which is sufficiently smaller than the event depth offset from the plate interface. Note that all of the tectonic features shown in Figure 10 come from the ocean bottom or marine seismic surveys. No results from a sole land seismic network are used in Figure 10 to avoid the misinterpretation of the spatial interrelationships. Further details of the tectonics at the off-Ibaraki region are discussed in the subsequent subsections.

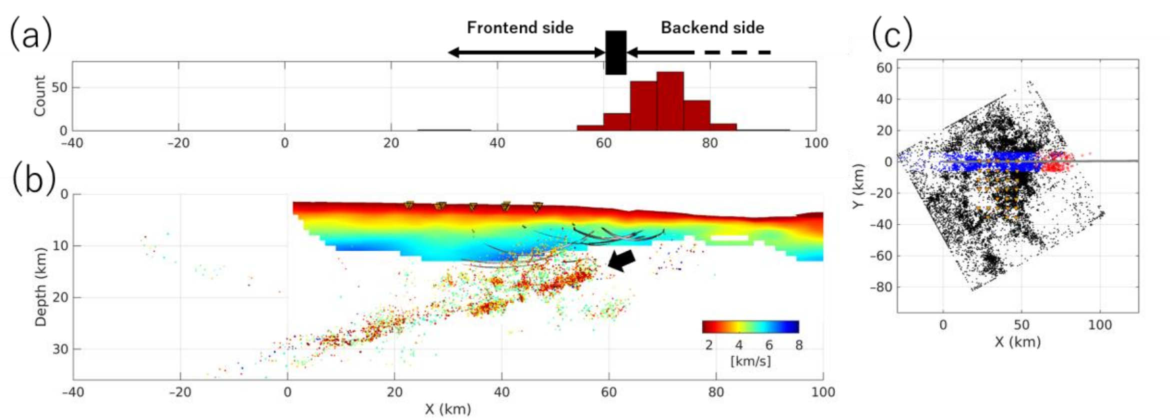

Figure 11. Integrated cross-sectional view at Line EW reported by Mochizuki et al. (2008). (a) Histogram of the number of tectonic tremors with Line EW (after the report by Nishikawa et al., 2019). The thick vertical bar denotes the coarse location of the top of the seamount. (b) P-wave velocity structure after Mochizuki et al. (2008). The gray convex curves present the intensity of the migrated reflection arrival times from the plate interface (Mochizuki et al., 2008). Hypocenters along Line EW from the present study are overlaid. The thick black arrow points to the planar downdip interface. The orange inverted triangles present the locations of OBSs. Colors of hypocenters show the days after the Mw7.9 event, as shown in Figure 9. (c) Plan view parallel to the survey line (X-axis) and perpendicular to the survey line (Y-axis). The horizontal gray bold line is the seismic survey line of Line EW reported by Mochizuki et al. (2008). The black dots represent all the hypocenters obtained from this study. The blue and red dots present the selected events for the depth profile shown in (b) and the selected tectonic tremors shown in (a). The events within 6 km from the seismic survey line were selected. The orange inverted triangles show the location of OBSs.

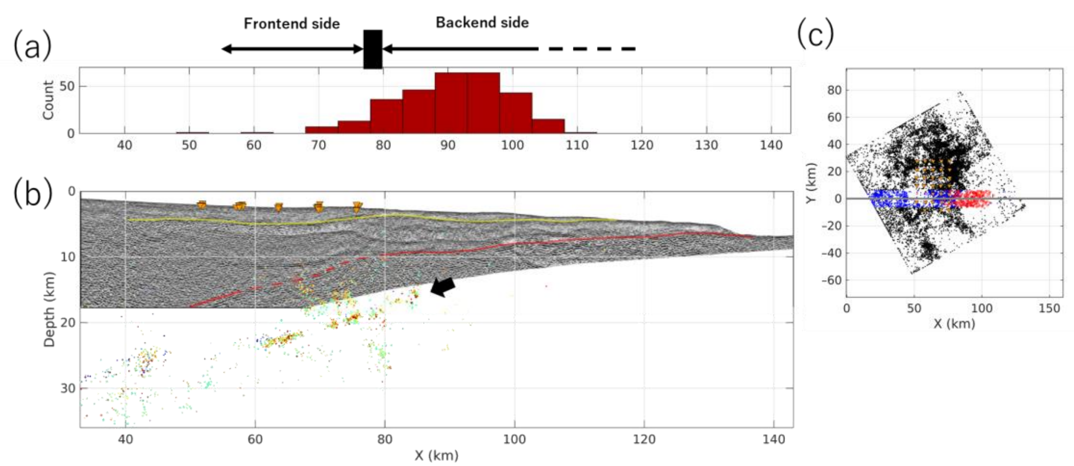

Figure 12. Integrated cross-sectional view at Line 13 reported by Tsuru et al. (2002). (a) Histogram of the number of tectonic tremors along Line 13 (after the report by Nishikawa et al., 2019). The thick vertical bar denotes the coarse location of the top of the seamount. (b) Seismic reflection profile reported by Tsuru et al. (2002). Hypocenters along Line 13 from the present study are overlaid. Colors of hypocenters show the days after the Mw7.9 event, as shown in Figure 9. The solid red and yellow lines present the interpreted top of igneous oceanic crust and the Cretaceous layer by Mochizuki et al. (2008), respectively. The thick black arrow points to the planar downdip interface. (c) Plan view parallel to the survey line (X-axis) and perpendicular to the survey line (Y-axis). The horizontal gray bold line is the seismic survey line of Line 13 reported by Tsuru et al. (2002). The black dots represent the hypocenters obtained from this study. The blue and red dots present the selected events for the depth profile shown in (b) and the selected tectonic tremor shown in (a). The events in which offset are smaller than 6 km were selected from the seismic survey line.

5.1 Seismicity overview concerning surrounding tectonics

The event distribution of this study showed that the high seismicity zone is concentrated at the front-end side of the seamount (Figures 10–12). By contrast, the seismicity is quite low around the top or back-end side of the seamount. In this low-seismicity zone, the shallow tectonic tremors are distributed with little spatial gap with small earthquakes. We focus on the spatial relationship between the seismogenic zone and the subducting seamount.

In the plan view of the seismicity shown in Figure 10, this high-seismicity zone showed a horizontal variation along the rim of the front-end side of the subducting seamount. The seismicity in the northern side is higher than that in the eastern or southern side. Nakatani et al. (2015) suggested that this zone is a part of the seamount. The spatial seismicity pattern in this study is consistent with this previous study. Nakatani et al. (2015) discussed that this horizontal and vertical seismicity variation along the rim of the seamount may be a consequence of a stress field change by the Mw7.9 event. On top of this consistency, this study can further discuss the event depth variation. The event depth variation clarifies that, temporally bounded by the occurrence of the Mw7.9 event, the depth variation of the seismicity changed considerably from a monotonic planar distribution (Figure 9a) to a depth-variant heterogeneous distribution (Figure 13). This seismicity suggests that subsurface structures are illuminated by the small earthquakes. Particularly, the presence of depth-variant subfaults and/or microfractures are shown around the seamount, including inside the oceanic crust.

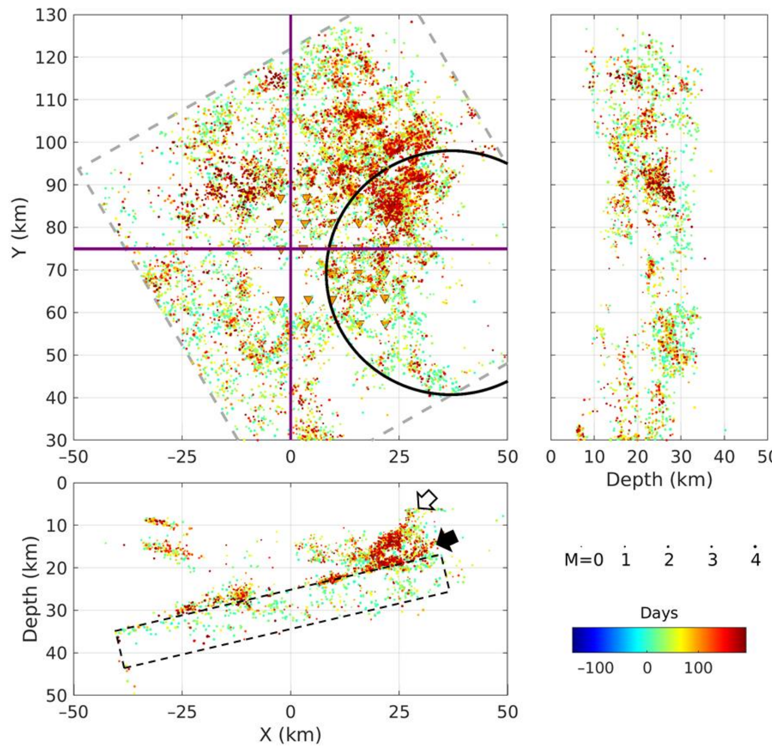

Figure 13. Same event and layout as shown in Figure 9b with additional notations. The solid open circle in the plain map view represents the seamount. The black and white arrows in the cross section denote the planar downdip interface and the high-angle downdip interface, respectively. The black dashed rectangle in the cross section denotes the temporally activated high-seismicity zone only for a few tens of days after the Mw7.9 event.

The updip limit of the seismogenic zone corresponds to ~10-km plate interface depth. This updip limit is located around the top of the subducting seamount. Using numerical modeling, Sun et al. (2020) showed that at around the top of the seamount, the effective normal stress along the plate interface is considerably smaller than the one along the front-end side. This updip limit located around the top of the seamount may be explained, at least partly, by this normal stress reduction that is incapable of generating stick-slip events along with the plate interface of the seamount (Sun et al., 2020). However, the interpretation of the resultant seismicity in this study is complicated due to the presence of two seismically active interfaces (Figure 13). To clarify the plate interface, in the next subsection, 5.2, we discuss the details of the gently sloped planar downdip interface—the most prominent interface identified in this study.

5.2 Planar downdip interface

The depth of the planar downdip interface is ~18 km at the updip limit of the seismogenic zone (Figure 13). This planar interface is also discernable by the hypocenter reported by Shinohara et al. (2011, 2012), which is around the same depth as that in the present study (Figure S7). This planar downdip interface had been active before the Mw7.9 event throughout the entire OBS experiment period. The latest large earthquake in this off-Ibaraki region before the 2011 Mw7.9 event was M7.0 event on 8 May 2008 (Takiguchi et al., 2011). This M7.0 event in 2008 also occurred at the deeper portion, and its rupture propagated from relatively deeper to a shallower direction (Takiguchi et al., 2011). The aftershock distribution of this M7.0 event in 2008 was examined by Yamada et al. (2011). The comparison of the event distribution is shown between the aftershocks of this M7.0 event in 2008 and the event distribution before the Mw7.9 event in 2011 determined in this study (Figure 14). In the plain map view of Figures 14a and 14b, the aftershocks of the M7.0 event in 2008 exhibit a similar spatial seismicity pattern as seismicity analyzed in the present study before the occurrence of the Mw7.9 event. The cross sections of both seismicities show a clear planar downdip trend. The aftershocks of Mw7.9 in 2011 reported by Shinohara et al. (2011, 2012) are consistent with these results. That is, the hypocenters reported by Yamada et al. (2011), Shinohara et al. (2011, 2012) and this study showed a consistent geometry for this planar downdip interface in spite of the different dataset and the different event location method. Therefore, we conclude that these planar downdip interfaces between 2008 and this study from 2010 to 2011 are the same seismic interfaces. If this is true, then it is natural to interpret that as an overall tendency, this planar downdip interface has been stably sliding for years from 2008 to 2011. The depth of this planar downdip interface is ~18 km at around the updip limit of the seismogenic zone.

Meanwhile, Yamada et al. (2011) also reported that there is a low-seismicity zone in the study area of the present study, which overlaps with the low-seismicity zone of the 2011 Mw7.9 event in the present study (Figure 14). This low-seismicity zone appears to be seismically inactive. Hence, this zone might be an exception of a stable sliding, which we will further discuss in section 5.5.

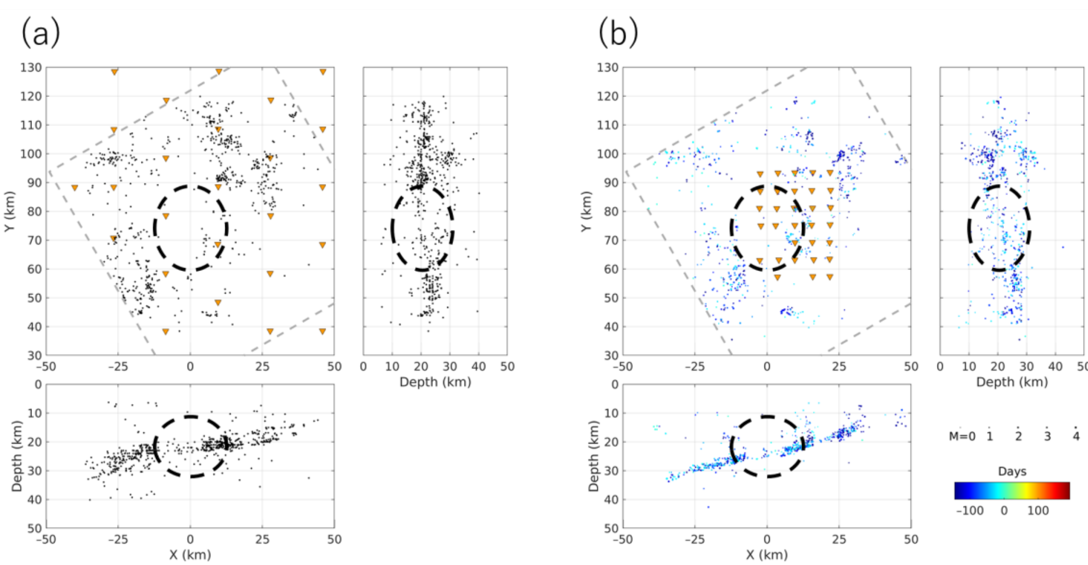

Figure 14. (a) Aftershock distribution of M7.0 event in 2008 (after Yamada et al., 2011). The orange inverted triangles present the OBS locations during 2008 aftershock observation (Yamada et al., 2011). The events within the study area of the present study are shown. Entire spatial range of events shown in the plan map was used for cross section. The bold dashed circles represent the low-seismicity zones of the 2011 Mw7.9 event. (b) Hypocenters in this study from 17 October 2010 to 11 March, 2011. The bold dashed circles represent the low-seismicity zones of the 2011 Mw7.9 event.

From the viewpoint of the geometry of this planar downdip interface and its temporal stability of the seismicity, this gently sloped planar downdip interface appears to be a plate interface of a subducting slab. However, it is questionable to conclude that this planar downdip interface is the plate interface as the top of the oceanic crust. As shown in Figures 10–12, the active source seismic surveys revealed that the depth of the plate interface as the top of the oceanic crust is ~10 km (Mochizuki et al., 2008; Tsuru et al., 2002) and not 18 km. Nishizawa et al. (2009) also performed a seismic survey close to the Line EW of Mochizuki et al. (2008) and showed that the plate interface depth at around the top of the seamount was ~13 km, a few kilometers deeper than that of Mochizuki et al. (2008). On one hand, Mochizuki et al. (2008) applied an active source seismic tomography for determining the velocity structure. Moreover, an arrival time migration method was applied to identify and determine the depth of the plate interface validated by a synthetic waveform. Nishizawa et al. (2009) applied a wide-angle refraction survey method to obtain the depth of the plate interface. Accordingly, it is difficult to directly examine the depth difference of the plate interface between these studies. However, the depths of the plate interface from these seismic surveys are considerably shallower than the event distribution of the planar downdip interface in this study.

The depth offset between the plate interdece from the seismic profile and the planar downdip interface from the small earthquakes is more evident at Line 13 (Figure 12) than the one at Line EW (Figure 11). At Line 13, the depth offset is ~8 km at around the top of the subducting seamount. This appears to be a discrepancy between the depth of the plate interface inferred from the event distribution and those obtained from the active source seismic surveys.

Because the Vp/Vs ratio was optimized for the event location in the present study, we believe that the event depth is hardly biased. To further examine the effect of velocity model error against the depth of the event location, we performed a set of event locations tests using different velocity models. The test conditions and results are presented in Table 1. The test result shows that the average event depth shift is at most 1.3 km. Even the nonoptimal Vp/Vs ratio of 1.78 does not explain the depature of event depth from the plat einterface. In addition, the event location of P-only dataset without using the S-wave hardly changed the average event depth below the OBS network. This supports that the S-wave velocity structure is accurate enough to constrain the event depths to our final results. Consequently, we conclude that the error of the velocity structure model is not the cause of the discrepancy between the depth of event location and the depth of plate interface using the active source seismic survey.

The remaining possibility that can cause the event depth error is the presence of an extremely low-velocity anomaly in a real velocity structure that was not incorporated in the velocity model, especially for the S-wave around the plate interface. However, we believe that such an anomaly is unrealistic. First, the P-only event location did not have such a shift. Second, to result in the 8 km of the depth shift, ~1.0 s of the $S - P$ time error must be accounted for throughout the study area (roughly assuming Vp = 6 km/s and Vs = 3.4 km/s). But past studies using the active source seismic surveys did not identify such a low-velocity layer (Mochizuki et al., 2008; Nakahigashi et al., 2012, Nishizawa et al., 2009; Tsuru et al., 2002). In this way, the velocity model error effect is difficult to explain this departure between the depth of the plate interface and the depth of events. Consequently, errors in the velocity structure are hard to explain this prominent depth offset between the top of the oceanic crust and the planar downdip interface.

Table 1. *Test Conditions of the Velocity Model Error Effect and Results.*

	Use of seismic phases	Vp/Vs ratio below the basement	Mean event depth [km]	Mean event depth shift [km]	Mean coherence
Reference velocity model	P&S	1.74 (optimal)	19.36	-	0.766 (best)
Reference velocity model	P-only	-	18.09	−1.27 km	0.833 (note: P-only)
Vp/Vs change	P&S	1.78	18.26	−1.10 km	0.764

5.3 High-angle dipping plane above the downdip planar interface

As presented in Figure 13, a high-angle dipping plane is identified above the downdip planar interface. The depth of this plane around the updip limit of the seismogenic zone is ~10 km. This depth appears to agree with the depth of the plate interface from seismic profiles. Therefore, this high-angle dipping plane could be a part of a plate interface. However, to avoid any misconclusion, we discuss the following two cases: 1) the planar downdip interface is the plate interface as the top of the oceanic crust (Figure 15a) and 2) the high-angle dipping plane is a part of the plate interface (Figure 15b).

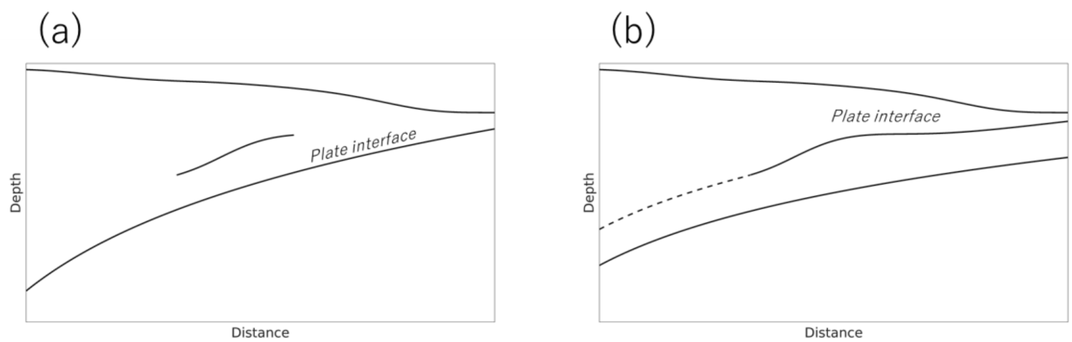

Figure 15. Diagrams showing the candidates of the plate interface. (a) Case showing that the planar downdip interface is the plate interface. (b) Case showing that the high-angle dipping plane is the plate interface.

5.3.1 Case 1: Planar downdip interface is the plate interface

In this case, the high-angle downdip interface is the subsurface structure above the plate interface. Wang and Bilek (2011, 2014) suggested that the subduction of the seamount causes microfractures in the overriding plate. As an alternative scenario, a cutting-off of the seamount from its base may be the other candidate for the consequence of the seamount subfuction (Cloos, 1992; Cloos & Shreve, 1996). Further, if this high-angle downdip interface is shallower than the top of the seamount, an out-of-sequence fault or accretionary wedge is perhaps the other candidate of a subsurface structure (e.g., Park et al., 2000). However, these structures are not identified in the off-Ibaraki region (Tsuru et al., 2002). Accordingly, in the particular case shown in Figure 15a, either microfractures or the cutting-off of the seamount may be the potential causes of the fracturing of the overriding plate which we further discuss below.

In microfractures and cutting-off scenarios, the planar downdip interface is supposed to be a plate interface. As discussed in the previous subsection, we suppose that the case presented in Figure 15a is less likely to occur. We raise a few additional factors that need further explanations for each microfracture and cutting-off scenario. First, the microfracture scenario does not explain why the shallow high-angle interface was activated only after the Mw7.9 event rather than a continual stable seismic activity. According to Wang and Bilek (2011), the microfracture is the consequence of a compressional stress against the overriding plate by a seamount subduction. The microseismicity associated with the microfractures is expected to occur continuously other than the aftershock. However, the observation in this study showed no such significant events above the plate interface. Second, if the planar downdip interface is the plate interface as the top of the oceanic crust, an explanation is needed why this interface does not exhibits no topological signature of the subducting seamount. Particularly in the case of the cutting-off scenario, an extra discussion is required if the base of the cutting-off interface is topologically smooth enough to cause a stable seismic activity even before the Mw7.9 event.

5.3.2 Case 2: High-angle downdip plane is the plate interface

The second case is that the high-angle dipping plane is a part of the plate interface (Figure 15b). The depth of this plane around the updip limit of the seismogenic zone is ~10 km. This is in reasonable agreement with the depth of the plate interface from the seismic survey (Figures 11 and 11). This case suggests that the events are dominant along or below the plate interface and not above. Conversely, previous studies on the seamount subduction anticipated that the seismicity on the overriding plate would be enhanced by developing microfractures (e.g., Sun et al., 2020; Wang and Bilek, 2011, 2014). No reasonable models appear to exist to explain the occurrence of the events below the plate interface in previous studies. Previous seamount subduction studies implicitly suggested that the oceanic plate is not fractured (see review by Wang & Bilek, 2014). Perhaps, the subducting oceanic plate is already fractured as reported in recent studies (e.g. Hino et al., 2009, Obana et al., 2021)

Most importantly in this case, one open question arises, i.e., how is the stable high seismicity of this planar dipping interface accounted for if it is deeper than the plate interface? As stated, this planar downdip interface seems stably sliding for years and it is a challenge to explain how such stable sliding of this interface persists for years below the oceanic crust. This topic is beyond the scope of this study and we cannot provide an answer for this question here. Further study is required, such as investigating a double-difference relocation and a seismic tomography for determining both P- and S-wave velocities to reveal the precise geometry of these interfaces and corresponding velocity structures.

5.4 Spatial boundary between earthquakes and shallow tectonic tremors

Shallower than the updip limit of the seismogenic zone, the tectonic tremors were identified using S-net (Nishikawa et al., 2019). These tremors were found after the deployment of S-net from 2016 to 2018 after the OBS experiment of this study. Meanwhile, shallow tectonic tremors were not identified during the OBS observation period. This is partly because of the difficulty in discriminating the signals of the tectonic tremors and those of the regional aftershocks of Tohoku-oki earthquake. Here, we assume that the tremor distribution is temporally steady enough not to invade the seismogenic zone.

The noticeable feature of the shallow tectonic tremor distribution is that this tremor is spatially complementary with the normal earthquakes bounded by the updip limit of the seismogenic zone (Figure 10–12). Kubo and Nishikawa (2020) showed that the rupture area of the Mw7.9 event and the subducting seamount are spatially complementary. Sun et al. (2020) showed that small-to-moderate earthquake occurs between the rupture area and the tectonic tremor. The present study agrees with Sun et al. (2020) with much precise manner that the spatial gap between the rupture area of the Mw7.9 event and the tremor is filled by small earthquakes located at the front- end of the seamount. The rupture area of the Mw7.9 event is discussed in the next subsection 5.5.

This spatial continuity between the small earthquakes and shallow tectonic tremors naturally suggests that the locations of these activities would be smoothly connected with the same or nearby interfaces. If this is true, it would be interesting and important to discuss what controls the boundary between this tectonic tremor and small earthquakes. The answer may not be as simple because as discussed in the previous subsection, the depth profile of the seismicity exhibited a variation along with the depth below the oceanic crust.

Regarding the shallow tectonic tremor, understanding the tremor generation mechanism is still in progress (e.g., Ide, 2021); however, extensive research is ongoing in subduction zones worldwide. Previous studies revealed that tectonic tremor comprises swarms of low-frequency earthquakes (LFEs) (Beroza & Ide, 2011; Nishikawa et al., 2019; Shelly et al., 2007). The duration of the tectonic tremor is approximately tens of seconds or longer (e.g., Nakano et al., 2019). The characteristic frequency content of LFEs is 1–8 Hz (Ide et al., 2007), which overlaps with those of the small earthquakes located in the study area (>4 Hz). This indicates that the tremor region is also seismogenic in the sense of radiating elastic energy at these high-frequency bands in the order of Hertz. From tectonic implications, the shallow tectonic tremors were shown to occur at the forefront of an accretionary wedge (Obana & Kodaira, 2009) or a shear zone around the décollement on the top of the oceanic crust (Hendriyana & Tsuji, 2021, Sugioka et al., 2012). This study follows these previous studies proposing that the shallow tectonic tremors occur along or in the vicinity of the plate interface.

However, these tectonic structures and tremor locations do not fit with the off-Ibaraki region because this region is characterized by the lack of décollement or an accretionary prism (Tsuru et al., 2002). According to the multichannel seismic survey, this earthquake-tremor boundary corresponds to the top of the seamount. No such subsurface structures are identified herein (Figures 11 and 12). Perhaps, other tectonic structures or mechanisms may be required to account for the tremor generation at the off-Ibaraki region.

Instead of the accretionary wedge or a shear zone around décollement, this study considers a case where the morphology of the subducting seamount surface gives control to define this seismogenic-tremor boundary. This discussion below is based on the numerical modeling study reported by Sun et al. (2020), showing that the effective normal stress around the top of the seamount is considerably smaller than that at the front-end side of the seamount.

As aforementioned, the updip limit of the seismogenic zone is located along ~10 km of isocontour of the plate interface depth. This 10-km contour is close to the top of the subducting seamount. According to Sun et al. (2020), a stress shadow may be generated along the plate interface at the shallow ward in the seamount's wake owing to the variation of the slope of the seamount morphology. Because this stress shadow is the region where the effective normal stress is considerably reduced, a shear slip around the top of the seamount's back-end side is easier to be initiated than that at the front-end side (Sun et al., 2020). In contrast with the back-end side of the seamount that can be a stress shadow region, at the front-end side of the seamount, the effective normal stress will be considerably larger compared with that in the shallow tremor region; hence, it is harder for the tectonic tremor to be initiated. Accordingly, it is implicated that the 10 km of the isodepth plate depth contour corresponding to a spatial boundary between the earthquakes and tectonic tremors is a boundary between the non-stress shadow and the stress shadow. This model presented by Sun et al. (2020) explains the boundary of the seismogenic and tremor region observed in this study even without the presence of an accretionary wedge or a décollement along the plate interface.

5.5 Semicircular low-seismicity zone and the largest Mw7.9 aftershock event

As shown in Figure 10, a large semicircular low-seismicity zone was identified. The size of this low-seismicity zone is ~30 km × 25 km along the strike and dip direction, respectively. The seismicity of this zone has been continuously inactive since the aftershock of 2008 M7.0 event as per the OBS observation (Figure 14a). The event detection capability is quite good in this low-seismicity zone; the event-detection lower limit at ~20-km depth is M0.5 (Figure 6). In this low seismicity zone, a tectonic tremor was not identified in this zone, especially before the Mw7.9 event. Because of these reasons, an extremely weak coupling condition along the fault plane is very unlikely in this low-seismicity zone.

Meanwhile, it is well known that the aftershocks occur around the rim of the main coseismic rupture area (e.g. Mendoza & Hartzell, 1988, Yagi et al., 1999). In the present study, the hypocenter of the Mw7.9 event was relocated around the western rim of the semicircular low-seismicity region underneath the OBS network (Figure 8). Nakatani et al. (2015) reported a consistent hypocenter of the Mw7.9 event. The rupture direction of the Mw7.9 event is known to have propagated toward updip from the hypocenter (Kubo et al., 2013; Suzuki et al., 2020). These results suggest that the semicircular low-seismicity zone corresponds to a part of the coseismic rupture area of the Mw7.9 event, possibly the main rupture area. The A-GPS survey (Honsho et al., 2019, Tomita et al., 2017) showed that in contrast to the Tohoku-oki region, the southern Japan trench region including off-Ibaraki region is characterized by an afterslip region after the 2011 Tohoku-oki earthquake. The A-GPS data in this off-Ibaraki region from 2012 to 2016 are shown in Figure 10. This A-GPS result suggests that the afterslip of the Mw7.9 event may have continued for years.

One may argue that the fault plane depth of the Mw7.9 thrust event is still controversial because there are two dipping planes of a planar downdip interface and high-angle downdip interface (Figure 15), hence the coseismic fault plane cannot be unambiguously specified. Actually, this study cannot provide a constraint regarding the depth of the fault planes. Further characterization such as a delta CFF analysis will provide a better insight into the fault plane of this Mw7.9 event.

6 Summary and conclusions

This study proposed a comprehensive workflow to apply the migration-based event location method proposed by Yoneshima and Mochizuki (2021) to the local small earthquakes recorded in OBSs at the off-Ibaraki region. This workflow includes the optimization of the input velocity model particularly for the Vp/Vs ratio below the basement of the sediment layer.

By applying this event location workflow, we have intensively located the small earthquakes for more than 20,000 events around the subducting seamount and the rupture area of the Mw7.9 event. The error bars for majority of events are smaller than ±2 km. The event detection capability in the study area ranged from approximately M1 to M4 that is practically enough to identify the high- and low-seismicity zones in the study area.

The event distribution showed noticeable seismicity patterns that are correlated with the surrounding tectonics. At the updip, bounded by the updip limit of the seismogenic zone, small earthquakes and shallow tectonic tremors were found to be spatially complementary. This boundary may be explained as the boundary between the stress shadow and non-stress shadow region in terms of the effective normal stress change that arose from the topological change of the subducting seamount, according to Sun et al. (2020).

At the deeper portion, a semicircular low-seismicity zone was identified beneath the OBS network. This zone was interpreted as the main coseismic rupture area of the Mw7.9 event in 2011, although the exact depth of the rupture fault plane is still uncertain.

A clear temporal change was identified bounded by the Mw7.9 event; the seismicity changed from a simple planar downdip interface to a depth-variant heterogeneous pattern with two distinct interfaces and a swarm-like scattered events below the planar downdip interface. The shape of a simple planar downdip interface is overall subparallel to the subducting slab identified from the active source seismic profiles. However, its depth was unexpectedly several kilometers deeper than the plate interface as the top of the oceanic crust. Our result showed that the temporally activated high-angle downdip interface after the Mw7.9 event agree with the plate interface depth determined from the seismic surveys. This also suggests that the planar downdip interface is deeper than the plate interface.

Acknowledgments

We thank the journal editor and anonymous reviewers for their comments and suggestions, which greatly improved the manuscript. The OBS seafloor experiment was supported by Japan’s Ministry of Education, Culture, Sports, Science and Technology (MEXT) under its Observation and Research Program for Prediction of Earthquakes and Volcanic Eruptions.

Open Research

The JMA Mw7.9 event in Figure 2 is from the JMA unified event catalog downloaded from the National Research Institute for Earth Science and Disaster Resilience Data Management Center (https://hinetwww11.bosai.go.jp/auth/?LANG=en) on March 23, 2021. The A-GPS data were obtained from the reports by Honsho et al. (2019), presented in the Supporting Information document. The shallow tectonic tremor catalog was obtained from the report by Nishikawa et al. (2019) in the section of Supplementary Material document. Most of the data analysis and figures were obtained using MATLAB R2020b. Some maps were created using Generic Mapping Tools version 4 (Wessel & Smith, 1995). The FMTOMO program code, used to compute travel times, was downloaded from http://www.iearth.org.au/codes/FMTOMO/download/ on 24, February, 2021. The error ellipsoid was drawn by a MATLAB function error_ellipse (Johnson, 2022). The hypocenter catalog determined in this study is available at

TBD_TO_BE_SPECIFIED_AFTER_THE_ACCEPTANCE. All the datasets used to make Figures are archived at https://zenodo.org/record/6371243 for peer review.

References

Arai, R., Kodaira, S., Yamada, T., Takahashi, T., Miura, S., Kaneda, Y., Nishizawa, A., & Oikawa, M. (2017). Subduction of thick oceanic plateau and high-angle normal-fault earthquakes intersecting the slab. *Geophysical Research Letters*, *44*(12), 6109–6115. https://doi.org/10.1002/2017GL073789

Bartal, Y., Somer, Z., Leonard, G., Steinberg, D. M., & Horin, Y. B. (2000). Optimal seismic networks in israel in the context of the comprehensive test ban treaty. *Bulletin of the Seismological Society of America*, *90*(1), 151–165. https://doi.org/10.1785/0119980164

Bassett, D., & Watts, A. B. (2015). Gravity anomalies, crustal structure, and seismicity at subduction zones: 2. Interrelationships between fore-arc structure and seismogenic behavior. *Geochemistry, Geophysics, Geosystems*, *16*(5), 1541–1576. https://doi.org/10.1002/2014GC005685

Beroza, G. C., & Ide, S. (2011). Slow earthquakes and nonvolcanic tremor. *Annual Review of Earth and Planetary Sciences*, *39*(1), 271–296. https://doi.org/10.1146/annurev-earth-040809-152531

Chesley, C., Naif, S., Key, K., & Bassett, D. (2021). Fluid-rich subducting topography generates anomalous forearc porosity. *Nature*, *595*(7866), 255–260. https://doi.org/10.1038/s41586-021-03619-8

Cloos, M. (1992). Thrust-type subduction-zone earthquakes and seamount asperities: A physical model for seismic rupture. *Geology*, *20*(7), 601–604. https://doi.org/10.1130/0091-7613(1992)020<0601:TTSZEA>2.3.CO;2

Cloos, M., & Shreve, R. L. (1996). Shear-zone thickness and the seismicity of Chilean- and Marianas-type subduction zones. *Geology*, *24*(2), 107–110. https://doi.org/10.1130/0091-7613(1996)024<0107:SZTATS>2.3.CO;2

Collot, J.-Y., Sanclemente, E., Nocquet, J.-M., Leprêtre, A., Ribodetti, A., Jarrin, P., Chlieh, M., Graindorge, D., & Charvis, P. (2017). Subducted oceanic relief locks the shallow megathrust in central Ecuador. *Journal of Geophysical Research: Solid Earth*, *122*(5), 3286–3305. https://doi.org/10.1002/2016JB013849

DeMets, C., Gordon, R. G., Argus, D. F., & Stein, S. (1990). Current plate motions. *Geophysical Journal International*, *101*(2), 425–478. https://doi.org/10.1111/j.1365-246X.1990.tb06579.x

de Kool, M., Rawlinson, N., & Sambridge, M. (2006). A practical grid-based method for tracking multiple refraction and reflection phases in three-dimensional heterogeneous media. *Geophysical Journal International*, *167*(1), 253–270. https://doi.org/10.1111/j.1365-246X.2006.03078.x

Earthquake Research Committee, Long-term evaluation of earthquakes Sanriku-oki to Boso-oki, in *Publications of Earthquake Research Committee—January–December 2011—*, edited by Earthquake Research Committee, The Headquarters for Earthquakes Research Promotion, 817 pp., 2012 (in Japanese).

Grigoli, F., Cesca, S., Amoroso, O., Emolo, A., Zollo, A., & Dahm, T. (2014). Automated seismic event location by waveform coherence analysis. *Geophysical Journal International*, *196*(3), 1742–1753. https://doi.org/10.1093/gji/ggt477

Hendriyana, A., & Tsuji, T. (2021). Influence of structure and pore pressure of plate interface on tectonic tremor in the Nankai subduction zone, Japan. *Earth and Planetary Science Letters*, *558*, 116742. https://doi.org/10.1016/j.epsl.2021.116742

Hino, R., Ito, S., Shiobara, H., Shimamura, H., Sato, T., Kanazawa, T., Kasahara, J., & Hasegawa, A. (2000). Aftershock distribution of the 1994 Sanriku-oki earthquake (Mw 7.7) revealed by ocean bottom seismographic observation. *Journal of Geophysical Research: Solid Earth*, *105*(B9), 21697–21710. https://doi.org/10.1029/2000JB900174

Hino, R., Azuma, R., Ito, Y., Yamamoto, Y., Suzuki, K., Tsushima, H., Suzuki, S., Miyashita, M., Tomori, T., Arizono, M., & Tange, G. (2009). Insight into complex rupturing of the immature bending normal fault in the outer slope of the Japan Trench from aftershocks of the 2005 Sanriku earthquake (Mw = 7.0) located by ocean bottom seismometry. *Geochemistry, Geophysics, Geosystems*, *10*(7). https://doi.org/10.1029/2009GC002415

Honda, R., Yukutake, Y., Ito, H., Harada, M., Aketagawa, T., Yoshida, A., Sakai, S., Nakagawa, S., Hirata, N., Obara, K., Matsubara, M., & Kimura, H. (2013). Rupture process of the largest aftershock of the M 9 Tohoku-oki earthquake obtained from a back-projection approach using the MeSO-net data. *Earth, Planets and Space*, *65*(8), 917–921. https://doi.org/10.5047/eps.2013.01.003

Honsho, C., Kido, M., Tomita, F., & Uchida, N. (2019). Offshore postseismic deformation of the 2011 tohoku earthquake revisited: Application of an improved GPS-acoustic positioning method considering horizontal gradient of sound speed structure. *Journal of Geophysical Research: Solid Earth*, *124*(6), 5990–6009. https://doi.org/https://doi.org/10.1029/2018JB017135

Ide, S. (2021). Empirical low-frequency earthquakes synthesized from tectonic tremor records. *Journal of Geophysical Research: Solid Earth*, *126*(12), e2021JB022498. https://doi.org/10.1029/2021JB022498

Ide, S., Shelly, D. R., & Beroza, G. C. (2007). Mechanism of deep low frequency earthquakes: Further evidence that deep non-volcanic tremor is generated by shear slip on the plate interface. *Geophysical Research Letters*, *34*(3). https://doi.org/10.1029/2006GL028890

Johnson, A. J. (2022). Error_ellipse (https://www.mathworks.com/matlabcentral/fileexchange/4705-error_ellipse), MATLAB Central File Exchange.

Kubo, H., Asano, K., & Iwata, T. (2013). Source-rupture process of the 2011 Ibaraki-oki, Japan, earthquake (Mw 7.9) estimated from the joint inversion of strong-motion and GPS data: Relationship with seamount and Philippine Sea Plate. *Geophysical Research Letters*, *40*(12), 3003–3007. https://doi.org/10.1002/grl.50558

Kubo, H., & Nishikawa, T. (2020). Relationship of preseismic, coseismic, and postseismic fault ruptures of two large interplate aftershocks of the 2011 Tohoku earthquake with slow-earthquake activity. *Scientific Reports*, *10*(1), 12044. https://doi.org/10.1038/s41598-020-68692-x

León-Ríos, S., Agurto-Detzel, H., Rietbrock, A., Alvarado, A., Beck, S., Charvis, P., Edwards, B., Font, Y., Garth, T., Hoskins, M., Lynner, C., Meltzer, A., Nocquet, J. M., Regnier, M., Rolandone, F., Ruiz, M., & Soto-Cordero, L. (2019). 1D-velocity structure and seismotectonics of the Ecuadorian margin inferred from the 2016 Mw7.8 Pedernales aftershock sequence. *Tectonophysics*, *767*, 228165. https://doi.org/10.1016/j.tecto.2019.228165

Lilwall, R. C., & Francis, T. J. G. (1978). Hypocentral resolution of small ocean bottom seismic networks. *Geophysical Journal of the Royal Astronomical Society*, *54*(3), 721–728. https://doi.org/10.1111/j.1365-246X.1978.tb05507.x

Matsubara, M., & Obara, K. (2011). The 2011 off the Pacific coast of Tohoku Earthquake related to a strong velocity gradient with the Pacific plate. *Earth, Planets and Space*, *63*(7), 663–667. https://doi.org/10.5047/eps.2011.05.018

Matsumura, S. (2010). Discrimination of a preparatory stage leading to M7 characteristic earthquakes off Ibaraki Prefecture, Japan. *Journal of Geophysical Research: Solid Earth*, *115*(B1). https://doi.org/10.1029/2009JB006584

Mendoza, C., & Hartzell, S. H. (1988). Aftershock patterns and main shock faulting. *Bulletin of the Seismological Society of America*, *78*(4), 1438–1449. https://doi.org/10.1785/BSSA0780041438

Miura, S., Kodaira, S., Nakanishi, A., Tsuru, T., Takahashi, N., Hirata, N., & Kaneda, Y. (2003). Structural characteristics controlling the seismicity crustal structure of southern Japan Trench fore-arc region, revealed by ocean bottom seismographic data. *Tectonophysics*, *363*(1), 79–102. https://doi.org/10.1016/S0040-1951(02)00655-8

Mochizuki, K., Nakahigashi, K., Kuwano, A., Yamada, T., Shinohara, M., Sakai, S., Kanazawa, T., Uehira, K., & Shimizu, H. (2010). Seismic characteristics around the fault segment boundary of historical great earthquakes along the Nankai Trough revealed by repeated long-term OBS observations. *Geophysical Research Letters*, *37*(9). https://doi.org/10.1029/2010GL042935

Mochizuki, K., Yamada, T., Shinohara, M., Yamanaka, Y., & Kanazawa, T. (2008). Weak interplate coupling by seamounts and repeating M ~ 7 earthquakes. *Science*, *321*(5893), 1194–1197. https://doi.org/10.1126/science.1160250

Nakahigashi, K., Shinohara, M., Mochizuki, K., Yamada, T., Hino, R., Sato, T., Uehira, K., Ito, Y., Murai, Y., & Kanazawa, T. (2012). P-wave velocity structure in the southernmost source region of the 2011 Tohoku earthquakes, off the Boso Peninsula, deduced by an ocean bottom seismographic survey. *Earth, Planets and Space*, *64*(12), 1149–1156. https://doi.org/10.5047/eps.2012.06.006

Nakajima, J., Hirose, F., & Hasegawa, A. (2009). Seismotectonics beneath the Tokyo metropolitan area, Japan: Effect of slab-slab contact and overlap on seismicity. *Journal of Geophysical Research: Solid Earth*, *114*(B8). https://doi.org/10.1029/2008JB006101

Nakanishi, A., Kodaira, S., Miura, S., Ito, A., Sato, T., Park, J.-O., Kido, Y., & Kaneda, Y. (2008). Detailed structural image around splay-fault branching in the Nankai subduction seismogenic zone: Results from a high-density ocean bottom seismic survey. *Journal of Geophysical Research: Solid Earth*, *113*(B3). https://doi.org/10.1029/2007JB004974

Nakano, M., Yabe, S., Sugioka, H., Shinohara, M., & Ide, S. (2019). Event size distribution of shallow tectonic tremor in the nankai trough. *Geophysical Research Letters*, *46*(11), 5828–5836. https://doi.org/10.1029/2019GL083029

Nakatani, Y., Mochizuki, K., Shinohara, M., Yamada, T., Hino, R., Ito, Y., Murai, Y., & Sato, T. (2015). Changes in seismicity before and after the 2011 Tohoku earthquake around its southern limit revealed by dense ocean bottom seismic array data. *Geophysical Research Letters*, *42*(5), 1384–1389. https://doi.org/10.1002/2015GL063140

Nishikawa, T., Matsuzawa, T., Ohta, K., Uchida, N., Nishimura, T., & Ide, S. (2019). The slow earthquake spectrum in the Japan Trench illuminated by the S-net seafloor observatories. *Science*, *365*(6455), 808–813. https://doi.org/10.1126/science.aax5618

Nishizawa, A., Kaneda, K., Watanabe, N., & Oikawa, M. (2009). Seismic structure of the subducting seamounts on the trench axis: Erimo Seamount and Daiichi-Kashima Seamount, northern and southern ends of the Japan Trench. *Earth, Planets and Space*, *61*(3), e5–e8. https://doi.org/10.1186/BF03352912

Obana, K., & Kodaira, S. (2009). Low-frequency tremors associated with reverse faults in a shallow accretionary prism. *Earth and Planetary Science Letters*, *287*(1), 168–174. https://doi.org/10.1016/j.epsl.2009.08.005

Obana, K., Kodaira, S., & Kaneda, Y. (2009). Seismicity at the eastern end of the 1944 Tonankai earthquake rupture area. *Bulletin of the Seismological Society of America*, *99*(1), 110–122. https://doi.org/10.1785/0120070236

Obana, K., Fujie, G., Yamamoto, Y., Kaiho, Y., Nakamura, Y., Miura, S., & Kodaira, S. (2021). Seismicity around the trench axis and outer-rise region of the southern Japan Trench, south of the main rupture area of the 2011 Tohoku-oki earthquake. *Geophysical Journal International*, *226*(1), 131–145. https://doi.org/10.1093/gji/ggab093

Park, J.-O., Tsuru, T., Kodaira, S., Nakanishi, A., Miura, S., Kaneda, Y., Kono, Y., & Takahashi, N. (2000). Out-of-sequence thrust faults developed in the coseismic slip zone of the 1946 Nankai earthquake (Mw=8.2) off Shikoku, southwest Japan. *Geophysical Research Letters*, *27*(7), 1033–1036. https://doi.org/10.1029/1999GL008443

Sachpazi, M., Kapetanidis, V., Charalampakis, M., Laigle, M., Kissling, E., Fokaefs, A., Daskalaki, E., Flueh, E., & Hirn, A. (2020). Methoni Mw 6.8 rupture and aftershocks distribution from a dense array of OBS and land seismometers, offshore SW Hellenic subduction. *Tectonophysics*, *796*(September), 228643. https://doi.org/10.1016/j.tecto.2020.228643

Sakai, S., Yamada, T., Shinohara, M., Hagiwara, H., Kanazawa, T., Obana, K., Kodaira, S., & Kaneda, Y. (2005). Urgent aftershock observation of the 2004 off the Kii Peninsula earthquake using ocean bottom seismometers. *Earth, Planets and Space*, *57*(4), 363–368. https://doi.org/10.1186/BF03352577

Sgroi, T., Polonia, A., Beranzoli, L., Billi, A., Bosman, A., Costanza, A., Cuffaro, M., D'Anna, G., de Caro, M., di Nezza, M., Fertitta, G., Frugoni, F., Gasperini, L., Monna, S., Montuori, C., Petracchini, L., Petricca, P., Pinzi, S., Ursino, A., & Doglioni, C. (2021). One year of seismicity recorded through ocean bottom seismometers illuminates active tectonic structures in the Ionian Sea (Central Mediterranean). *Frontiers in Earth Science*, *9*, 643. https://doi.org/10.3389/feart.2021.661311

Shaddox, H. R., & Schwartz, S. Y. (2019). Subducted seamount diverts shallow slow slip to the forearc of the northern Hikurangi subduction zone, New Zealand. *Geology*, *47*(5), 415–418. https://doi.org/10.1130/G45810.1

Shelly, D. R., Beroza, G. C., & Ide, S. (2007). Non-volcanic tremor and low-frequency earthquake swarms. *Nature*, *446*(7133), 305–307. https://doi.org/10.1038/nature05666

Shinohara, M., Yamada, T., Nakahigashi, K., Sakai, S., Mochizuki, K., Uehira, K., Ito, Y., Azuma, R., Kaiho, Y., Shiobara, H., Hino, R., Murai, Y., Yakiwara, H., Sato, T., Machida, Y., Shinbo, T., Isse, T., Miyamachi, H., Obana, K., Takahashi, N., Kodaira, S., Kaneda, Y., Hirata, K., Yoshikawa, S., Obara, K., Iwasaki, T., & Hirata, N. (2011). Aftershock observation of the 2011 off the Pacific coast of Tohoku earthquake by using ocean bottom seismometer network. *Earth, Planets and Space*, *63*(7), 835–840. https://doi.org/10.5047/eps.2011.05.020

Shinohara, M., Machida, Y., Yamada, T., Nakahigashi, K., Shinbo, T., Mochizuki, K., Murai, Y., Hino, R., Ito, Y., Sato, T., Shiobara, H., Uehira, K., Yakiwara, H., Obana, K., Takahashi, N., Kodaira, S., Hirata, K., Tsushima, H., & Iwasaki, T. (2012). Precise aftershock distribution of the 2011 off the Pacific coast of Tohoku earthquake revealed by an ocean-bottom seismometer network. *Earth, Planets and Space*, *64*(12), 8, 1137–1148. https://doi.org/10.5047/eps.2012.09.003

Shinohara, M., Hino, R., Yoshizawa, T., Nishino, M., Sato, T., & Suyehiro, K. (2005). Hypocenter distribution of plate boundary zone off Fukushima, Japan, derived from ocean bottom seismometer data. *Earth, Planets and Space*, *57*(2), 93–105. https://doi.org/10.1186/BF03352553

Sugioka, H., Okamoto, T., Nakamura, T., Ishihara, Y., Ito, A., Obana, K., Kinoshita, M., Nakahigashi, K., Shinohara, M., & Fukao, Y. (2012). Tsunamigenic potential of the shallow subduction plate boundary inferred from slow seismic slip. *Nature Geoscience*, *5*(6), 414–418. https://doi.org/10.1038/ngeo1466

Sun, T., Saffer, D., & Ellis, S. (2020). Mechanical and hydrological effects of seamount subduction on megathrust stress and slip. *Nature Geoscience*, *13*(3), 249–255. https://doi.org/10.1038/s41561-020-0542-0

Suzuki, W., Aoi, S., Sekiguchi, H., & Kunugi, T. (2020). Rupture processes of the 2011 Tohoku-Oki earthquake and its Two M7-vlass aftershocks derived using curved fault models. *Report of the National Research Institute for Earth Science and Disaster Resilience*, *84*(January), 1-16.

Takemura, S., Furumura, T., & Maeda, T. (2015). Scattering of high-frequency seismic waves caused by irregular surface topography and small-scale velocity inhomogeneity. *Geophysical Journal International*, *201*(1), 459–474. https://doi.org/10.1093/gji/ggv038

Takemura, S., Kobayashi, M., & Yoshimoto, K. (2016). Prediction of maximum P- and S-wave amplitude distributions incorporating frequency- and distance-dependent characteristics of the observed apparent radiation patterns. *Earth, Planets and Space*, *68*(1), 166. https://doi.org/10.1186/s40623-016-0544-8

Takiguchi, M., Asano, K., & Iwata, T. (2011). The comparison of source models of repeating subduction-zone earthquakes estimated using broadband strong motion records. *Zisin (Journal of the Seismological Society of Japan. 2nd Ser.)*, *63*(4), 223–242, (in Japanese with English abstract). https://doi.org/10.4294/zisin.63.223

Tomita, F., Kido, M., Ohta, Y., Iinuma, T., & Hino, R. (2017). Along-trench variation in seafloor displacements after the 2011 Tohoku earthquake. *Science Advances*, *3*(7), e1700113. https://doi.org/10.1126/sciadv.1700113

Tsuru, T., Park, J.-O., Miura, S., Kodaira, S., Kido, Y., & Hayashi, T. (2002). Along-arc structural variation of the plate boundary at the Japan Trench margin: Implication of interplate coupling. *Journal of Geophysical Research: Solid Earth*, *107*(B12), ESE 11-1-ESE 11-15. https://doi.org/10.1029/2001JB001664

Uhrhammer, R. A. (1980). Analysis of small seismographic station networks. *Bulletin of the Seismological Society of America*, *70*(4), 1369–1379. https://doi.org/10.1785/BSSA0700041369

Yagi, Y., Kikuchi, M., Yoshida, S., & Sagiya, T. (1999). Comparison of the coseismic rupture with the aftershock distribution in the Hyuga-nada Earthquakes of 1996. *Geophysical Research Letters*, *26*(20), 3161–3164. https://doi.org/https://doi.org/10.1029/1999GL005340

Yamada, T., Nakahigashi, K., Kuwano, A., Mochizuki, K., Sakai, S., Shinohara, M., Hino, R., Murai, Y., Takanami, T., & Kanazawa, T. (2011). Spatial distribution of earthquakes off the east coast of the Kanto region along the Japan Trench deduced from ocean bottom seismographic observations and their relations with the aftershock sequence of the 2011 off the Pacific coast of Tohoku earthquake. *Earth, Planets and Space*, *63*(7), 60. https://doi.org/10.5047/eps.2011.06.045

Yamaya, L., Mochizuki, K., Akuhara, T., & Nishida, K. (2021). Sedimentary structure derived from multi-mode ambient noise tomography with dense OBS network at the Japan Trench. *Journal of Geophysical Research: Solid Earth*, *126*(6), e2021JB021789. https://doi.org/https://doi.org/10.1029/2021JB021789

Yarce, J., Sheehan, A. F., Nakai, J. S., Schwartz, S. Y., Mochizuki, K., Savage, M. K., Wallace, L. M., Henrys, S. A., Webb, S. C., Ito, Y., Abercrombie, R. E., Fry, B., Shaddox, H., & Todd, E. K. (2019). Seismicity at the northern Hikurangi Margin, New Zealand, and investigation of the potential spatial and temporal relationships with a shallow slow slip event. *Journal of Geophysical Research: Solid Earth*, *124*(5), 4751–4766. https://doi.org/10.1029/2018JB017211

Yoneshima, S., Mochizuki, K., Araki, E., Hino, R., Shinohara, M., & Suyehiro, K. (2005). Subduction of the Woodlark Basin at New Britain Trench, Solomon Islands region. *Tectonophysics*, *397*(3–4), 225–239. https://doi.org/10.1016/j.tecto.2004.12.008

Yoneshima, S., & Mochizuki, K. (2021). Migration-based local event-location workflow for ocean-bottom seismometer (OBS) records in subduction zones: A practical approach for addressing a large number of events. *Bulletin of the Seismological Society of America*. https://doi.org/10.1785/0120210109

Wang, K., & Bilek, S. L. (2011). Do subducting seamounts generate or stop large earthquakes? *Geology*, *39*(9), 819–822. https://doi.org/10.1130/G31856.1

Wang, K., & Bilek, S. L. (2014). Invited review paper: Fault creep caused by subduction of rough seafloor relief. *Tectonophysics*, *610*, 1–24. https://doi.org/10.1016/j.tecto.2013.11.024

Watanabe, H., 1971. Determination of earthquake magnitude at regional distance in and near Japan, Zisin. *J. Seismol. Soc. Jpn*., *24*, 189–200, (in Japanese with English abstract).

Wessel, P., & Smith, W. H. F. (1998). New, improved version of generic mapping tools released. *Eos, Transactions American Geophysical Union*, *79*(47), 579. https://doi.org/10.1029/98EO00426

Zhou, Z., Cheng, R., Rui, Y., Zhou, J., Wang, H., Cai, X., & Chen, W. (2020). An improved onset time picking method for low SNR acoustic emission signals. *IEEE Access*, *8*, 47756–47767. https://doi.org/10.1109/ACCESS.2020.2977885

References From the Supporting Information

Smith, W. H. F., & Wessel, P. (1990). Gridding with continuous curvature splines in tension. *Geophysics*, *55*(3), 293–305. https://doi.org/10.1190/1.1442837

Journal of Geophysical Research, Solid Earth

Supporting Information for

Precise hypocenter distribution in and around the subducting seamount, Mw7.9 thrust event, and shallow tectonic tremor at the off-Ibaraki region, the southern part of northeast Japan

Shinji Yoneshima[1], Kimihiro Mochizuki[1], Tomoaki Yamada[1], and Masanao Shinohara[1]

[1]Earthquake Research Institute, University of Tokyo.

Contents of this file

Figures S1 to S9.

Introduction

This supporting information provides a supplemental description of the basic ocean bottom seismometer (OBS) experiment information and quality control of the event location processing result. Figure S1 presents the OBS experiment period for each OBS. Figure S2 depicts the Vp/Vs ratio of the sediment layer estimated from the PS-converted wave. Figure S3 presents a waveform example of a local event. Figure S4 presents Magnitude plots between the JMA magnitude and the OBS magnitude. Figure S5 shows the M-T diagram to present the lower limit's temporal change of the event magnitude detection. Figure S6 is the histogram of the error bar for the located events. Figure S7 presents the hypocenters from Shinohara et al. (2011, 2012). Figures S8 and S9 present the cross section of the error ellipsoid along with the seismic survey line of Line EW (Mochizuki et al. 2008) and Line 13 (Tsuru et al., 2002).

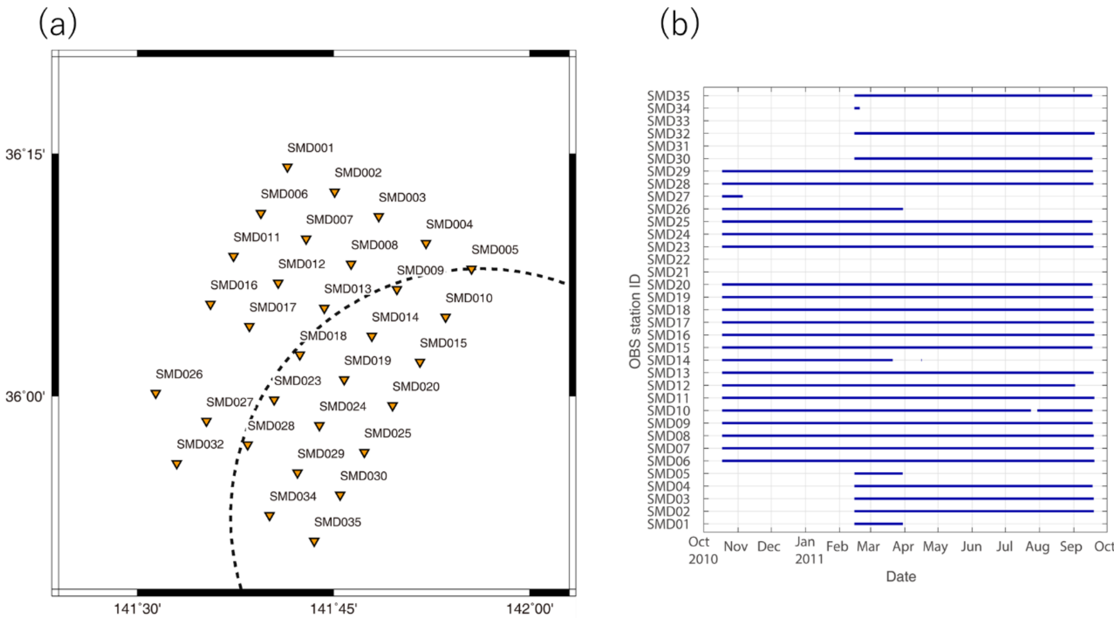

Figure S1. Label names of OBSs and observation period. (a) Plan map view with station labels. (b) Observation period of each OBS.

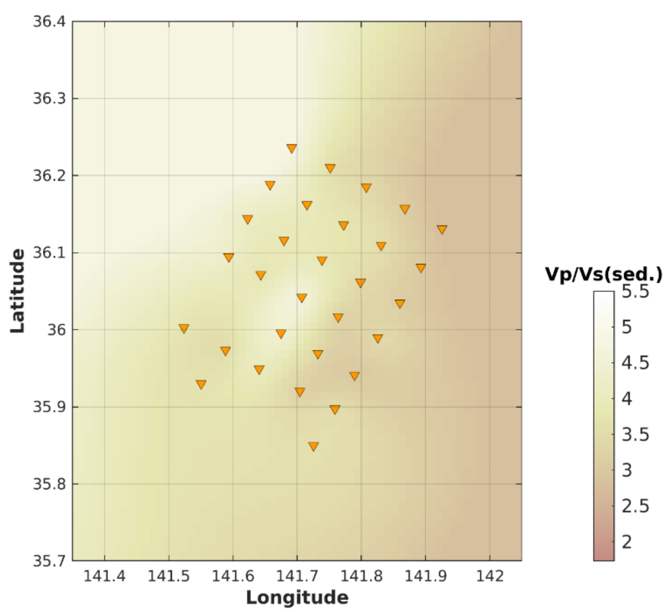

Figure S2. Estimated Vp/Vs ratio distribution in the sediment layer. The spatial interpolation that preserves an exact value just below the OBS site was applied (Smith & Wessel, 1990).

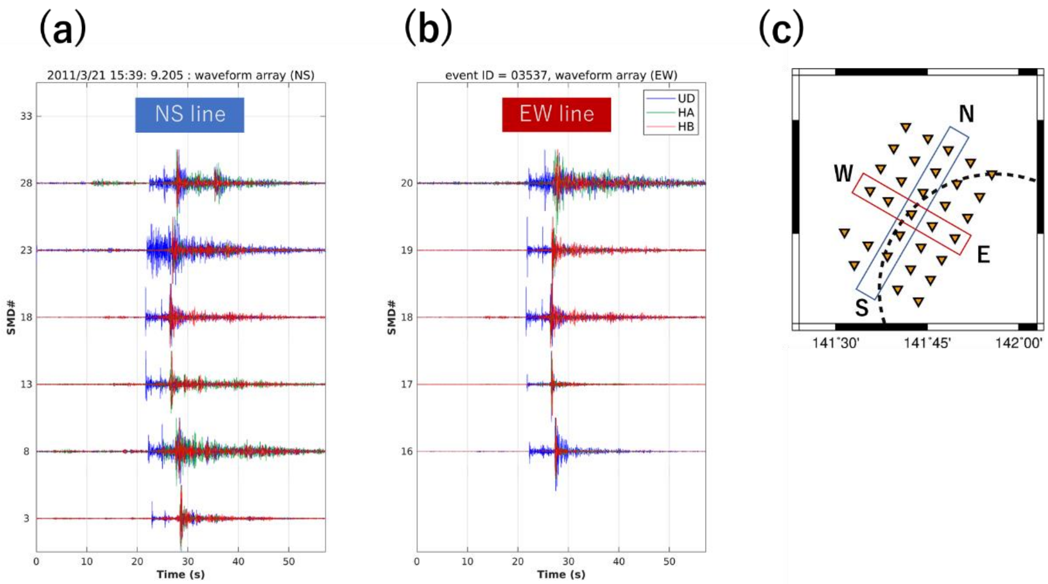

Figure S3. Example of the waveform recorded by OBSs. Each component of the waveform traces is normalized by the maximum amplitude. (a) North-south (NS) OBS arrays. Three-component waveforms are presented. (b) East-west (EW) OBS arrays. (c) Plan view of the OBS network showing the NS and EW arrays.

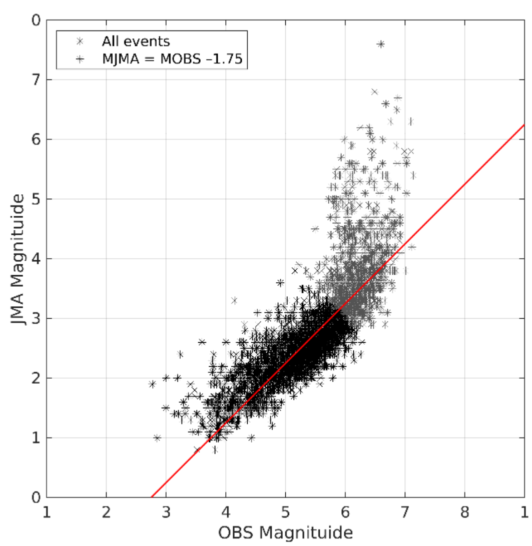

Figure S4. Uncorrected OBS magnitude versus JMA magnitude. The red line denotes thecorrection function after a line fit. The gray stars represent all the available events. The number of samples (N) is 3448. The black stars are the selected events for the fitting (N = 2467).

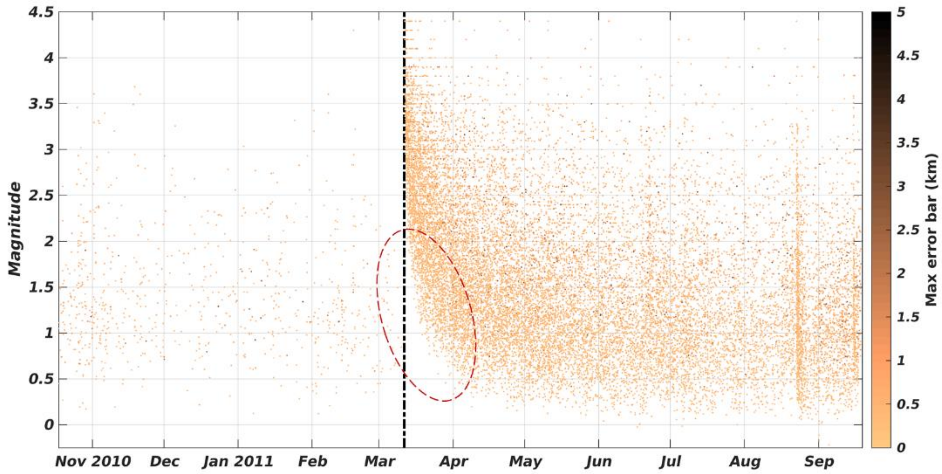

Figure S5. M-T diagram. The color of each dot denotes the error bar of the event. The vertical dot-dashed line presents the origin time of the 2011 Tohoku-oki earthquake. The red dashed circle presents the region of the degraded event detection performance.

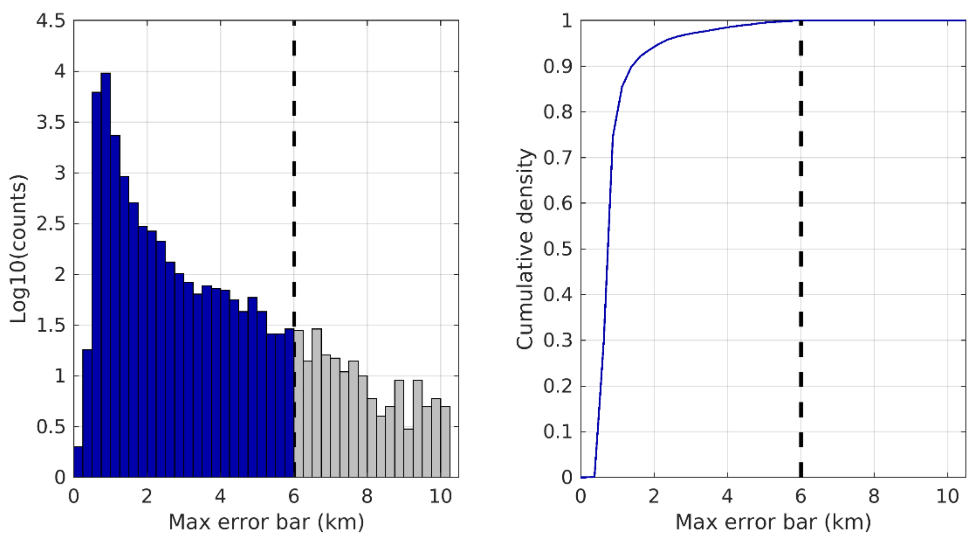

Figure S6. Error bar distribution. (Left) Histogram of the error bar with 95% confidence interval. Gray and dark blue bars are the error bars of the selected events within ±6km error bar, and all the events before the selection, respectively. The number of events before and after the selection are 22,562 and 21,242, respectively. The vertical dashed bar is the criteria of the event selection. (Right) Cumulative summation of the histogram.

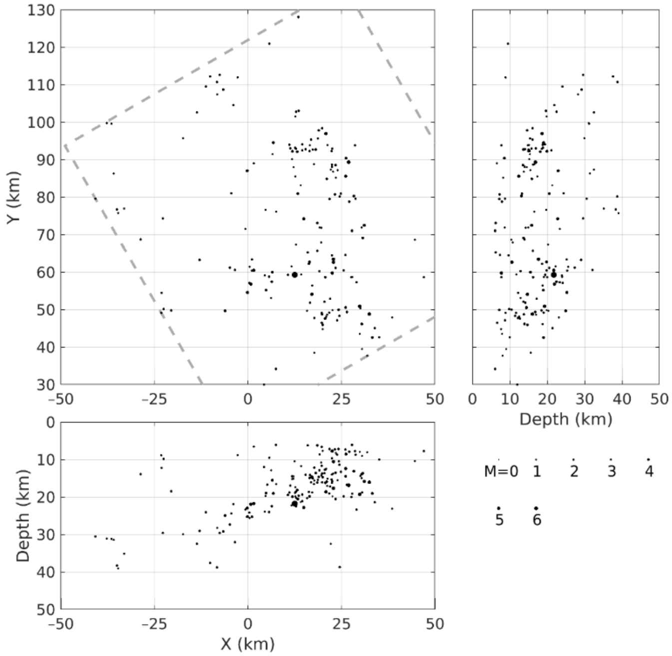

Figure S7. Cross-sectional view of the hypocenters (after Shinohara et al. 2011, 2012). The gray dashed rectangular area shows the study area used in this study.

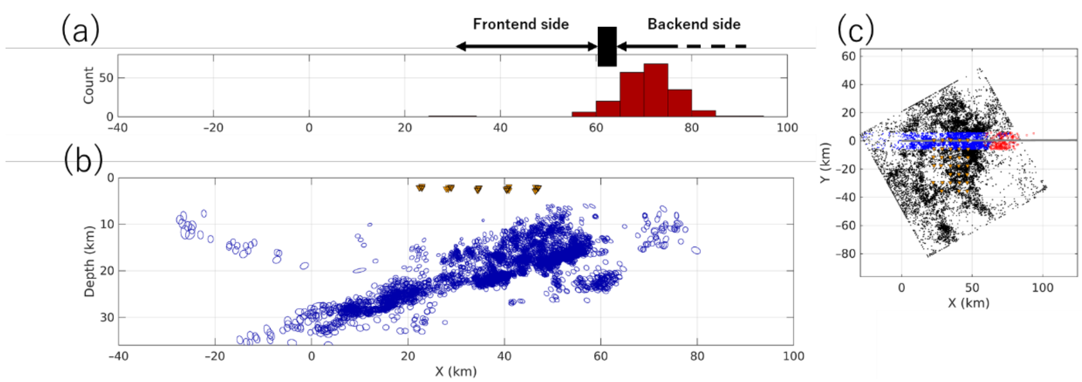

Figure S8. Error ellipsoids of events presented in Figure 10. (a) Same plot with Figure 10a. (b) Error ellipsoids of 68 % confidence interval for events shown in Figure 10b. (c) Same plot with Figure 10c.

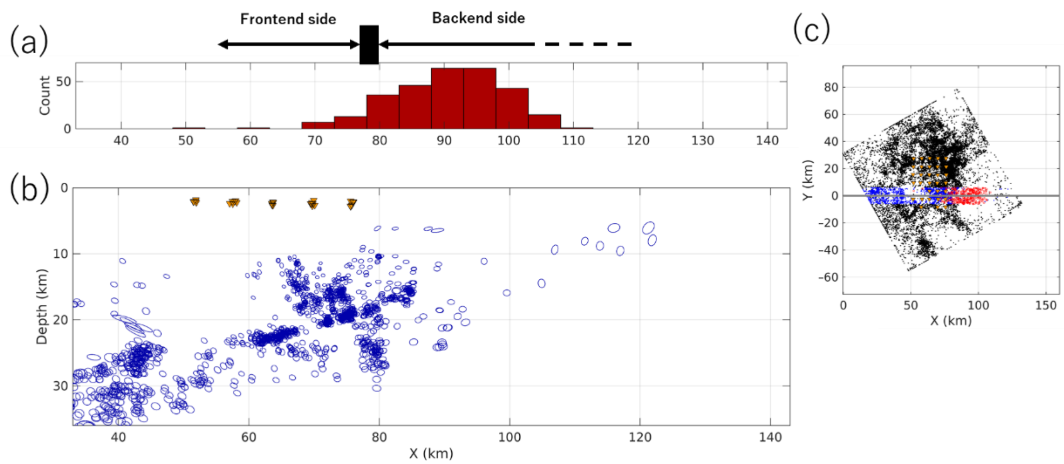

Figure S9. Error ellipsoids of events in presented Figure 11. (a) Same plot with Figure 11a. (b) Error ellipsoids of 68 % confidence interval for the events shown in Figure 11b. (c) Same plot with Figure 11c.